CMOS MEMS Oscillator for Gas Chemical Detection

by

Sarah Bedair

Master's Project Report

in

Electrical & Computer Engineering

at

Carnegie Mellon University

Advisor: Professor Gary Fedder

Second Reader: Professor David Lambeth

December, 2004

Abstract

This work describes the fabrication and testing of a CMOS/MEMS electrostatically self-excited cantilever based resonator gas detector under various gas exposures. CMOS/MEMS fabrication of a mass sensitive gas detector allows for integration with CMOS circuitry potentially leading to fully integrated sensor arrays of different physical modalities for organic vapors and biological agents. Such an environmental sensor will be portable, cheap, and small compared to other non-integrated gas detection methods.

The cantilever resonator includes a 100 μm square platform for the chemically sensitive receiver layer used in this work, polystyrene. The polymer is deposited using a drop-on-demand inkjet, an attractive technique due to its low cost and ease of processing. The ability of casting precise amounts of different sensitive materials combined with fully integrated mass sensitive oscillator electronics is a potential technology for single chip electronic noses and "lab on chip" applications.

The device was tested with and without 2.3 pL of polystyrene. Nitrogen gas saturated with methanol, ethanol, 2-propanol, and acetone gases was flowed over the device and gas concentration sensitivities of -4.56, -9.14, -

10.21, and -8.54 x 10^{-5} Hz/ppm, respectively, were found. Theoretically, a higher limit of ethanol gas sensitivity of - 0.03 Hz/ppm was estimated for the current device with a maximum achievable polystyrene volume, 54 pL, that can deposited onto the device. Further improvements for future designs are proposed with an estimated sensitivity of -0.37 Hz/ppm, which is a three order of magnitude improvement over the current device.

1 Introduction: MEMS Chemical Sensors

1.1 Motivation

Since the early 1990's microelectromechanical systems (MEMS) has been a growing field and since its inception has prevailed in several areas and applications such as inertial sensors, ink-jet printers, optical switches, RF communications, and chemical sensing. Specifically, chemical sensing research has been an expanding field for the past twenty years. There are many applications for chemical sensors such as environmental sensing, industrial monitoring, quality control, process applications in the food industry, and medical applications [1]. Full on-chip integration using CMOS/microelectromechanical systems (MEMS) technology provides a viable means for such chemical sensing applications because of its inherent qualities that lead to

device miniaturization, low power consumption, high signal to noise ratio, low cost, and total system portability. Potential products include 'electronic noses', which are gas sensing arrays, and 'electronic tongues', which are liquid sensing arrays.

1.2 Chemical Sensors and Sensing Modalities

Chemical sensors are implemented by interfacing a chemically sensitive layer to a transducer. The operation of the sensor is based upon the fact that a reversible chemical change upon absorption of, chemical reaction with, or charge transfer with a chemical species induces a change in the physical properties of the sensitive layer. Such changes include mass, volume, resistance, stress, optical properties, and heat exchange. Chemical sensing transducers may be arranged into six main categories: calorimetric or thermal sensors, electrochemical sensors, conductive sensors**,** stress sensors, optical sensors, and gravimetric (or mass-sensitive) sensors. For the particular sensing modality, transduction between the chemical absorption domain to an electrical signal domain such as frequency, current, or voltage change, takes place [2]. The

current work focuses on the gravimetric sensing modality using a micro-resonator fabricated using a CMOS/MEMS process.

1.3 Gravimetric Chemical Sensors

1.3.1 Mass-sensitive Sensors

Any chemical species that may accumulate onto a chemically sensitive surface may be detected with a mass-sensitive sensor. Common mass-sensitive devices utilize piezoelectric quartz substrates. These include the thickness shear mode resonator (TSMR), also known as quartz micro-balance (QMB) [3][11], and the Rayleigh surface acoustic wave (SAW) device [12]. Other devices use cantilever mass sensors [2]. TSMR and the SAW device are commercially available and commonly used for volatile organic compound detection. Detection of humidity, mercury vapor, and volatile organic compounds are some common applications of cantilever mass sensors [4]. Cantilevers have also been used for biomolecular recognition in a liquid media [9].

1.3.2 Cantilever Mass Sensors

Most mass-sensitive micro-cantilevers consist of a simple beam, where many designs have a relatively large plate connected to the free cantilever end to accommodate coating with a chemically sensitive layer. There are two modes of operation: measurement of static deflection from expansion or contraction of the layer due to chemical absorption [9][10] and dynamic measurement of resonance frequency shift due to mass loading [2]. In the static mode, the analyte absorption onto the surface of the cantilever induces heat producing thermal stress as well as mechanical stress changes from receptor chemistry swelling. These phenomena cause the cantilever to bend and deflect on the nanometer scale. The static mode requires soft and long cantilevers. Transducer detection in previous works requires an optical setup for monitoring cantilever deflection [2]. The dynamic mode requires shorter and stiffer cantilevers for a higher resonance quality factor and, therefore, good frequency stability. Dynamic mode excitation may be implemented by exciting the cantilever by piezoelectric, magnetic, electrostatic, or thermal bimorph actuation. For an overview of these different actuation types see references [2] and [13]. This report focuses on the dynamic mode electrostatic excitation and detection.

1.3.3 Selectivity, Sensitivity, and Limits of Detection (LOD)

For our work polymers were chosen as the chemical receptor layer. Gas sensor selectivity depends on the certain polymer receptor chemistry chosen to be deposited onto the device. Through proper selection of polymer coatings, a range of partial selectivities due to polymer-analyte absorption properties may be exploited. Different polymers may be utilized on similar cantilever devices in a device array configuration. The CMOS MEMS technology is advantageous with respect to arraying devices due to the small device dimensions, and the ability to implement the interface electronics and electronic multiplexing on chip. Such a configuration allows for a complete system on a single chip with analyte discrimination because an array of polymers with differing partial selectivities to different analytes will impose a certain signal "tag" for a specific analyte. Implementation of this arrayed configuration is out of the scope of this work, but is a topic for further improvements to the current gas detection scheme.

Cantilever mass sensors have inherently high mass sensitivity due to the small mass of the cantilever itself. A few pico-grams is the absolute resolution of such gas sensors. This has been determined for differing geometries as well as for differing operation modes (static and dynamic) by several authors (see

[4] for a review of the area). Such a high device mass sensitivity (Hz/g) does not necessarily imply a high gas concentration sensitivity (Hz/ppm) since the gas sensitivity is proportional to both the device mass sensitivity as well as the chemical receptor analyte sensitivity (g/ppm) of the chemical receptor deposited on the device. A larger mass of analyte will accumulate into a large volume of receptor polymer that has a high affinity for the specific analyte. For cantilever mass sensors, the area of the chemical receptor layer exposed to the analyte is relatively small, i.e. on the order of 100 μm by 150 μm or smaller, compared to TSMR and SAW devices which are traditionally much larger. Since the polymer volume exposed relative to the transducer volume is smaller than that in TSMR and SAW devices, the overall absorbed mass compared to the transducer volume will be relatively small in cantilever mass sensors [2]. Therefore, there is an important trade-off between high resolution and sensitivity of a cantilever and the small dimensions of the cantilever. Resolution and sensitivity are inversely proportional to one another and an efficient gas sensor design should be guided by an optimum combination of the two given the constraints of the system. It is imperative that the ratio of chemical receptor mass to the transducer mass and, subsequently, the analyte to transducer mass ratio be as large as possible. This will lead to a highly sensi-

tive gas concentration sensor which will respond to a particular gas concentration level even in ppm or ppb. High resolution mass sensors are also of interest in micro gas analyzers where the analyte is pre-concentrated prior to detection. The pre-concentration gain is typically on the order of 1000. In particular, gas chromatograph systems utilize small sample sizes and so the finite residence time for detection is small. However, for continuous gas sensing applications where a pre-concentrator is impractical, a concentration sensor is of interest.

Although the small dimensions of the cantilever adversely affects the gas concentration sensitivity, such sensors show comparable performance with respect to limits of detection and thermal stability to TSMR and SAW devices [4]. Also, direct compatibility with electronics and potential inclusion of other transducer sensing modalities on the same chip allows for a compact gas detection system as well as potentially lower minimum detectable signal levels. Lange et al. reported polyetherurethane (PEUT) coated cantilevers (with dimensions on the order of 100 x 150 μm^2 and 100 x 500 μm^2) with sensitivities of -0.10 and -0.01 Hz/ppm for toluene and ethanol, respectively [4]. In this report, a sensitivity of -0.9 x 10-5 Hz/ppm to ethanol was measured experimentally for our devices. The theoretical limit of sensitivity for the cur-

rent device using polystyrene is calculated to be -0.002 Hz/ppm. Our devices will exhibit lower gas concentration sensitivities due to lower transducer mass size and, therefore, mass sensitivity. However, by simple optimization of physical sizing of the current device configuration a predicted sensitivity of -0.02 Hz/ppm may be achieved. Higher sensitivity levels may also be achieved through the use of other polymer chemical receptors.

Lange et al. also compared their cantilever properties with PEUT coated TSMR and SAW devices [5]. Their limit of detection (LOD) to n-octane was 2.8 ppm. This is comparable to a LOD of 1.5 ppm and 7ppm of n-octane for the TSMR and SAW devices, respectively. Baller et al. used cantilevers with a length, width, and thickness of 500 μm, 100 μm, and 1 μm, respectively and they estimated a sub-ppm limit of detection for propanol using the cantilever in deflection mode [6]. They implemented the cantilever in both static deflection and dynamic modes by monitoring the displacement with the use of a laser and they used piezoelectric actuation for the dynamic excitation [7]. Jesenius et al. [8] also implemented a cantilever with length, width, and thickness of 200 μm, 50 μm, and 2 μm, respectively, in deflection mode and reported an estimated limit of detection of 10 ppm for ethanol. An absolute limit of detection for the current device in this report has not been evaluated because the

frequency stability of the device has yet to be explored, but this is recognized as an important metric for gas sensors.

1.4 CMOS MEMS Micromachining

The current work illustrates a mass-sensitive cantilever fabricated in a standard CMOS process. This device is electrostatically actuated while mechanical motion transduction to the electrical domain takes place through capacitive detection. Microstructures in the CMOS chip were released using a few maskless etching steps compatible with on-chip circuitry [14]. The details of the process are illustrated in Figure 1.1. The microstructures are fabricated using Jazz Semiconductor Inc. 0.35 mm BiCMOS [15] and Taiwan Semiconductor Manufacturing Company (TSMC) 0.35 mm CMOS [16] processes. The post-CMOS micro-machining involves etching the top dielectric layer down to the aluminum electrodes and a subsequent undercutting of the structures by a Si etch (Figure 1.1). In the last stage of processing, the chemical receptor layer is deposited from solution using drop-on-demand ink jetting. In the current work, polystyrene polymer is used as the receptor chemistry. Ink jet printing is extremely attractive due to the ease of future device manufac-

turability and low cost. Such a deposition system allows precise amounts of solute, cast in a solvent, to be deposited onto the mass sensor. Once the drops are deposited onto the device and dried, the receptor chemistry layer remains on the resonator. Multiple chemical sensitive layer chemistries can be selectively deposited onto individual arrayed transducers with this approach.

This report first introduces the theory behind absorption of gases in receptor sensitive polymers and the concepts of our resonant cantilevers as gas sensors in Chapter 2. Chapter 3 describes the experimental results of the gas exposure tests on two devices: one with and one without polystyrene. Subsequently, Chapter 4 summarizes and compares the theory with experimental results and a discussion of further improvements for an optimal gas sensor is made.

FIGURE 1.1 *CMOS Post Processing and Gas Sensor Manufacturing Steps*

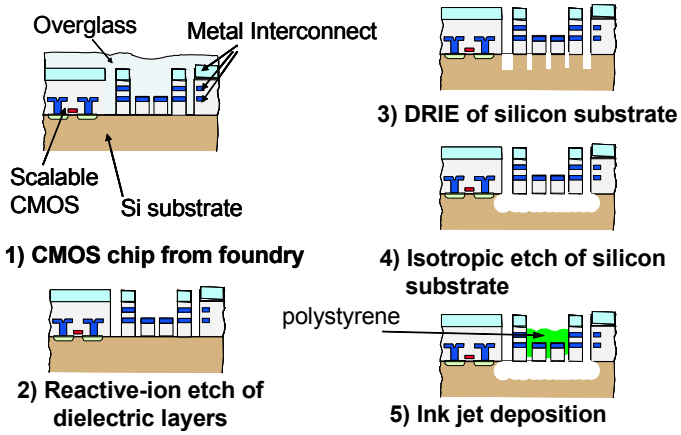

2 CMOS MEMS Gravimetric Sensors

2.1 Mechanical Resonators as Mass Sensors

Our work involves the analysis of a cantilever in operation at its fundamental resonant frequency. Figure 2.1 depicts the current resonator device structural layout. The resonator consists of a cantilever attached to a target end plate. The end plate is used to hold the receptor chemistry polymers. The electrostatic comb finger drives (top) actuate the resonator into motion. The comb finger capacitive motion detectors (bottom) sense differential motion generated current once the device is actuated. These sensing comb fingers are connected to a pre-amplifier on chip which converts the motion generated current to a voltage usable off chip.

FIGURE 2.1 *Resonator device illustration*

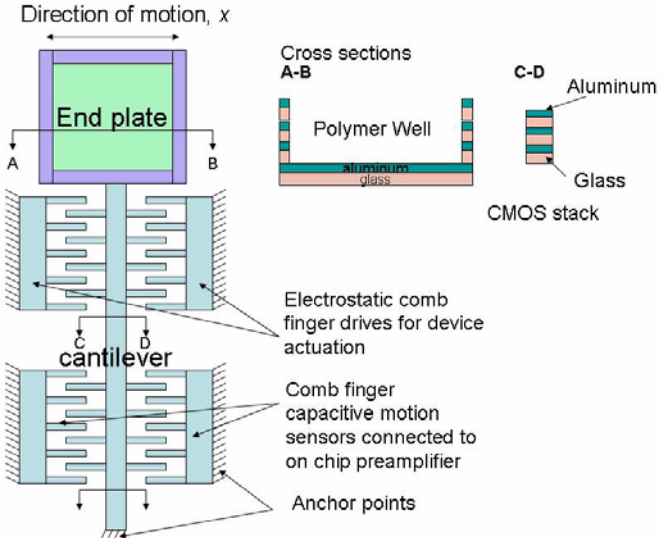

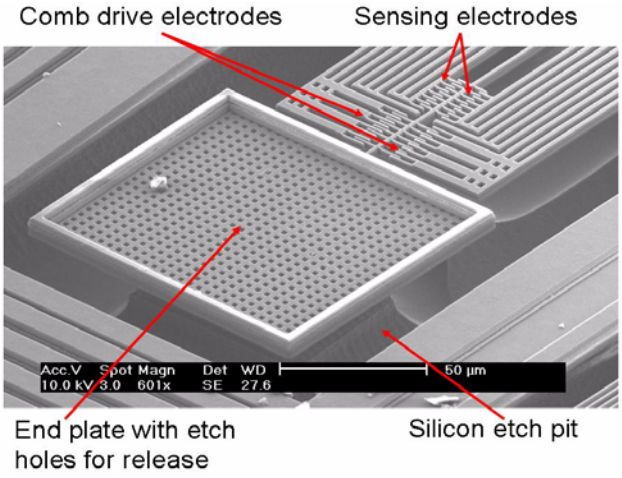

FIGURE 2.2 *SEM of our device*

Figure 2.2 shows our device before a receptor chemistry polymer has been deposited. The end plate dimensions are approximately 100 µm x 100 µm. Our device cantilever has width of 1.8 µm and length of 120 µm. Experimentally with these dimensions our device operates at a 5.8 kHz resonant frequency with a Q = 56. From (3.1) the calculated spring constant, *k,* is 0.298 N/m and the mass is calculated from (2.5) to be 65 ng.

Resonating cantilevers are modeled as classic mass spring damper systems as shown in Figure 2.3. In the figure *k* represents the spring constant, *B* is the damping coefficient, and *m* is the effective mass. The total force induced upon this system has a component accelerating the mass, one stretch-

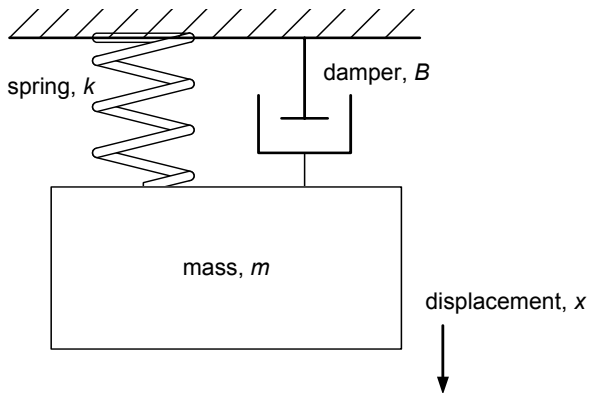

FIGURE 2.3 *Mass Spring Damper System*

ing or compressing the spring which is proportional to the spring constant and the displacement, x, of the mass, and a third component, the damping force that is proportional to the velocity, v, of the mass. The total external force is equal to the sum of these three reaction forces

$$F_{ext} = ma + Bv + kx \tag{2.1}$$

where a is the acceleration of the mass. By taking the Laplace transform of the above equation, the force response in the frequency domain is

$$F_{ext}(s) = m \cdot s^2 X(s) + B \cdot sX(s) + kX(s) \tag{2.2}$$

$$H(s) = \frac{X(s)}{F_{ext}(s)} = \frac{1}{m \cdot s^2 + B \cdot s + k} \tag{2.3}$$

where $H(s)$ is the mass-spring-damper system transfer function. This is a two-pole system with the poles at locations

$$p_{1,2} = -\frac{B}{2m} \pm \sqrt{\left(\frac{B}{2m}\right)^2 - \frac{k}{m}} \tag{2.4}$$

with natural frequency,

$$f_r = \frac{1}{2\pi}\sqrt{\frac{k}{m}} \tag{2.5}$$

and the quality factor

$$Q = \frac{\sqrt{mk}}{B} \tag{2.6}$$

To operate the mechanical resonator as a gravimetric device a chemically sensitive layer coating the mass of the system is added to the device using a drop on demand ink jet printing system. This layer has different affinities for differing analytes to be absorbed. A resonance shift is induced by mass loading of an analyte upon absorption to the chemically sensitive layer applied to the mass in the system. Such a phenomenon may be evaluated by taking the derivative of f_r with respect to the mass

$$\frac{df}{dm} = -\frac{1}{4\pi}\sqrt{\frac{k}{m^3}} \tag{2.7}$$

The frequency shift, Δf, for small applied mass change, Δm, is evaluated to be

$$\Delta f = -\frac{f_o}{2m}\Delta m \tag{2.8}$$

where f_o is the resonance frequency before mass adsorption. It is apparent that the lower the mass of the resonator the higher sensitivity (Hz/gram of added mass) is achieved. The minimum detectable frequency shift is based upon the thermal vibration of the cantilever which represents thermal noise. The following derivation for this minimum frequency shift is extracted from [19]. The cantilever motion induced by thermal energy may be described by the equipartition theorem

$$\frac{1}{2}m\omega_o^2\langle z^2{}_{\text{th}}\rangle = \frac{1}{2}k_B T \tag{2.9}$$

where $\langle z^2{}_{\text{th}}\rangle$ is the mean-square cantilever displacement at the end of the cantilever at the resonant frequency, $\omega_o = 2\pi f_o$, T is the temperature, and k_B is Boltzman's constant. The spectral noise density, $N_{\text{th}}(\omega)$, is related to the mean-square displacement by

$$\langle z^2{}_{\text{th}}\rangle = \frac{1}{2\pi}\int_0^\infty N_{\text{th}}(\omega)d\omega \tag{2.10}$$

and is described by [19]

$$N_{\text{th}}(\omega) = |H(s)|^2\Psi_{\text{th}}(\omega) \tag{2.11}$$

where the thermal white noise spectral density, $\Psi_{\text{th}}(\omega)$, is

$$\Psi_{\text{th}}(\omega) = \frac{4m\omega_o k_B T}{Q} \tag{2.12}$$

and $H(s)$ is written as

$$|H(s)|^2 = \frac{\left(\frac{1}{m^2}\right)}{(\omega_o^2 - \omega^2)^2 + \left(\frac{\omega_o \omega}{Q}\right)^2} \tag{2.13}$$

where $s \to j\omega$. The thermal noise at a frequency, $\omega_{\text{mod}} = \omega_o - \omega$, arises from the thermal noise $N_{\text{th}}(\omega)$ and may be approximated as

$$N_{\text{th}}(\omega) = \frac{k_B T}{m\omega_o Q \omega_{\text{mod}}^2} \tag{2.14}$$

for

$$\omega_{\text{mod}} \ll \omega_o \tag{2.15}$$

since (2.13) evaluates to

$$|H(s)|^2 = \frac{\left(\frac{1}{m^2}\right)}{4\omega_o^2 \omega^2_{mod} - 4\omega_o \omega^3_{mod} + \omega^4_{mod} + \left(\frac{\omega_o}{Q}\right)^{2\,2}} \tag{2.16}$$

$$|H(s)|^2 \approx \frac{\left(\frac{1}{m^2}\right)}{4\omega_o^2 \omega^2_{mod}}. \tag{2.17}$$

There is an apparent quality factor, Q', during oscillation with feedback. The oscillator concept will be explained in Section 2.6. This quantity is related to Q by

$$\frac{Q'}{Q} = \frac{\langle z^2_{\text{osc}} \rangle}{\langle z^2_{\text{th}} \rangle} \tag{2.18}$$

where $\langle z^2_{\text{osc}} \rangle$ is the mean-square displacement of the cantilever at driven oscillation. The phase noise energy, $E_{\text{P}}(\omega_{\text{mod}})$, and the cantilever oscillator energy, E_{c}, are

$$E_{\text{P}}(\omega_{\text{mod}}) = \frac{kN_{\text{th}}(\omega)}{2} \tag{2.19}$$

and

$$E_{\text{c}} = k\langle z^2_{\text{osc}} \rangle, \tag{2.20}$$

respectively. The mean-square frequency modulation, $\langle (\delta\omega)^2 \rangle$, induced by the thermal noise is evaluated by integrating over the bandwidth of measurement, ω_{BW},

$$\langle (\delta\omega)^2 \rangle = \frac{1}{2\pi} \int_{\omega_{BW}} \frac{2E_{\text{P}}(\omega_{\text{mod}})}{E_{\text{c}}} \omega^2_{\text{mod}} d\omega_{\text{mod}} \tag{2.21}$$

to yield

$$\langle (\delta\omega)^2 \rangle = \frac{\omega_{\text{o}} k_{\text{B}} T \omega_{\text{BW}}}{kQ\langle z^2_{\text{osc}} \rangle}. \tag{2.22}$$

The absolute minimum detectable mechanical shift in frequency is [20]

$$(\Delta f)_{min} = \frac{2}{X_o}\sqrt{\frac{f_o k_B T f_{BW}}{kQ}} \tag{2.23}$$

where X_o is the oscillation amplitude, k the spring constant, Q the mechanical quality factor, and f_{BW} the measurement bandwidth. By combining (2.8) and (2.23), the minimum detectable mass is

$$(\Delta m)_{min} = \frac{4m}{X_o}\sqrt{\frac{k_B T f_{BW}}{f_o kQ}} \tag{2.24}$$

Using the experimentally determined values of f_{BW} = 1Hz, k = 0.298 N/m, f_o = 5.8 kHz, Q = 56, T = 298 K, k_B = 1.38 x 10^{-23} J/K, m = 65 ng, and an oscillation amplitude, X_o, of 90 nm the minimum detectable frequency and mass shift based on thermal noise induced on the resonator are calculated to be 0.03 Hz and 0.6 pg, respectively.

There are other sources of noise associated with the total system (described in Section 2.5 through Section 2.7) which consists of the cantilever, the on-chip preamplifier, and external electronics. These components will introduce noise that may dominate the thermally induced noise on the cantilever. The noise associated with these components will not be discussed, but it should be noted that (2.23) describes the ultimate minimum measurable fre-

quency shift of the system and, therefore, minimum detectable concentration. The minimum detectable concentration concept is discussed in Section 2.3.2.

2.2 Gas Permeability and Solubility in "Glassy" Polystyrene Polymers

The particular sensitive polymer layer used in this work is polystyrene, which has the structural repeating unit shown in Figure 2.4

FIGURE 2.4 *Polystyrene Repeating Unit*

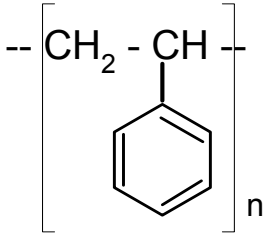

Polystyrene is a synthetic polymer used in applications such as disposable food containers, insulation, toothbrush handles, and Styrofoam [25]. This polymer is characterized by its good electrical insulation characteristics, low water absorption, and is also facile to produce. This material is resistant to organic acids, alkali, salts, and lower molecular weight alcohols, but readily absorbs hydrocarbons, esters, ketones (acetone is a ketone), and essential oils

[26]. The following represents the corresponding structural units of esters, ketones, and alcohols

FIGURE 2.5 *Ester, ketone, and alcohol function units*

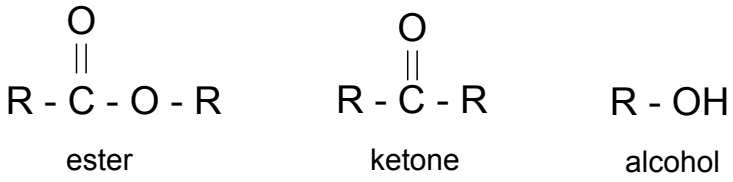

where R is a functional unit. The polystyrene, cast in a 1:1 toluene: xylene solution, is deposited onto the current mass sensitive device using drop-on-demand ink jet deposition [27]. Once the solvent in the solution coating the end plate evaporates a polystyrene film is left behind. The quantity of polystyrene deposited may be estimated accordingly with knowledge of the concentration of the cast solution, the number of drops placed on the device, as well as the volume of each drop (for a 30 μm jet purchased from [27] the jetted drop diameter is estimated to be ~ 30 - 50 μm with a volume ranging between 1.4 and 6.5 x 10^{-14} m^3).

In order to properly estimate the gas analyte absorption into the polymer films, information is needed on the particular gas vapor pressure, boiling point, and gas molecular size. Also, particular gas polymer interactions may

be predicted with some idea of the polymer molecular weight, size, glass transition temperature, and degree of amorphous versus crystalline phases inherent to the polymer structure.

2.2.1 Diffusivity, Permeability, and Solubility of Gases in a Polymer Medium

The permeation of small gas molecules into a polymer depends on the diffusivity and solubility of the gas in the particular polymer. The diffusion of gas through a polymer medium may be described by Fick's Law

$$\frac{dr}{dt} = DA\frac{dc}{dx} \tag{2.25}$$

with corresponding units of

$$\left(\frac{\text{molecules}}{\text{sec}}\right) = \left(\frac{\text{m}^2}{\text{sec}}\right)(\text{m}^2)\left(\frac{\text{molecules/m}^3}{\text{m}}\right), \tag{2.26}$$

where r the rate of the amount of matter passing through a unit area, A, under the influence of a concentration gradient, dc/dx. The proportionality factor, D, is the concentration independent diffusivity or diffusion coefficient and, according to the Arrhenius relationship, is temperature dependent as shown in the following

$$D \propto \exp\left(-\frac{E_D}{RT}\right), \tag{2.27}$$

where E_D is the diffusion activation energy (in Joules or Pa m^3), R the gas constant (8.314 Pa m^3/mol K), and T the temperature. To obtain concentration in moles the following is used

$$1\,\text{mol} = 6.022 \times 10^{23}\,\text{molecules}. \tag{2.28}$$

At equilibrium, the Bunsen solubility constant, *S,* describes the volume of gas per unit volume of the medium the gas is penetrating at a given pressure [28] [29]. Its dimensions are

$$\frac{\text{cm}^3(\text{STP})}{\text{cm}^3 \cdot \text{bar}} = \frac{10^{-5}\text{m}^3(\text{STP})}{\text{m}^3 \cdot \text{Pa}}. \tag{2.29}$$

where cm^3(STP) is the amount of gas in cm^3 at standard pressure and temperature (273 K and 1 bar = 10^5 Pa). Henry's Law relates the volume concentration (cm^3 of gas/cm^3 of polymer) of the gas, c, to unit partial pressure, p, of the gas [28][29] as

$$c = S \cdot p \tag{2.30}$$

$$S \propto \exp\left(-\frac{\Delta E_s}{RT}\right) \tag{2.31}$$

where ΔE_s is the change in enthalpy when the gas dissolves in the polymer.

Gas permeability, κ, is the rate at which a unit volume of gas passes through a medium of unit thickness per unit area at a certain pressure difference. Its dimensions are

$$\frac{\mathrm{cm}^3(\mathrm{STP})}{\mathrm{cm}\cdot\mathrm{s}\cdot\mathrm{bar}} = \frac{10^{-9}\mathrm{m}^3(\mathrm{STP})}{\mathrm{m}\cdot\mathrm{s}\cdot\mathrm{Pa}} \tag{2.32}$$

Permeability, diffusivity, and solubility are related by

$$\kappa = D \cdot S \tag{2.33}$$

[28][29]. The permeability of water (@ 25 C, 90% relative humidity) in polystyrene is 12,000 $\left(\frac{\mathrm{cm}^3\cdot\mathrm{cm}}{\mathrm{cm}^2\cdot\mathrm{mm\ Hg}\cdot\mathrm{sec}}\right)$ [26].

Gas sorption into “glassy” polymers is modeled to take place in two different modes: ordinary dissolution and "hole" filling [28]. The “hole” filling occurs when molecules are adsorbed into voids while ordinary absorption occurs in the amorphous portions of the polymer. Therefore, the total concentration of the gas molecules in the polymer may be separated into two components: the concentration of molecules in the holes, C_H, and the concentration of molecules actually absorbed, C_D. Therefore, the concentration of the analyte in a polymer medium can be considered as the combination of the following

$$C = C_H + C_D \tag{2.34}$$

$$C = \frac{C'_H b p_o}{1 + b p_o} + S p_o \tag{2.35}$$

where b is the hole affinity constant (Pa $^{-1}$) and p_o is the equilibrium pressure (Pa). The first term in the above equation represents the concentration of the gas molecules in the "holes" where as the second term represents regular dissolution of the gas which obeys (2.30).

The amorphous versus crystalline properties of the medium also affect the solubility of the gas. Absorption into a completely amorphous material is much more facile than into a crystalline material. Therefore, the degree of crystallinity affects the solubility constant in the following manner

$$S = \alpha S^* \tag{2.36}$$

where α is the amorphous volume fraction of the material and S^* is the solubility constant in a completely amorphous material [28]. For polystyrene, the density of its purely amorphous state versus the density of its crystalline state is reported to be 0.93 in [29]. Therefore, the amorphous volume fraction is calculated to be ~ 0.5 since the ratio of the two states is approximately 1:1 and the ratio of the volume of the amorphous state to the total volume is 1:2.

The degree of crystallinity of the polystyrene cast in solution and deposited onto the current device using our ink jet system has not been properly

determined and will have some variations between drops deposited at different times. The dropping environment, temperature, and humidity may vary from day to day. Also, the distance of the ink jet nozzle above the surface of the device may vary from experiment to experiment. All of these variations will lead to variations in the degree of crystallinity of the deposited polystyrene.

To a first-order approximation for amorphous polymers, the expected solubility (cm^3/cm^3*bar) of a gas is a function of the boiling point of the gas and is estimated by (@ T = 298 K) [29]

$$\log S = -2.1 + 0.0123 \cdot T_b \tag{2.37}$$

where T_b (in Kelvin) is the boiling point of the gas. Some of the vapor pressures and corresponding boiling points of the particular gas chemical substances utilized in this work are shown in Table 2.1.

2.2.2 Thermodynamic Partition Coefficient

In the environment, the behavior and absorption of a chemical substance between and into different media, such as air, water, and solid organic materials may be described by the partition coefficient [32]. This coefficient is spe-

TABLE 2.1 *Boiling Points, Vapor Pressures, and Expected Solubilities of Pertaining Chemical Substances [30]*

Chemical	T_b (K)	Vapor pressure @ 25 °C (mm Hg)	Vapor Pressure (bar)	Expected Maximum Volume Concentration in partially crystalline polystyrene ($cm^3$of gas/ $cm^3$of polystyrene)
methanol	337.75	126.77	0.169	9.575
ethanol	351.44	59.03	0.079	6.57
2-propanol (IPA)	355.45	45.15	0.060	5.63
acetone	329.15	231.03	0.308	13.68
water	373.15	23.76	0.032	4.81

cific to the chemical substance and the particular medium in which it is immersed and describes the equilibrium concentration of the substance in the corresponding media.

The partial pressure, P_B, of a single gas chemical substance "B", is related to the mole fraction, X_B, i.e. the number of moles of the gas analyte, n_B,versus the total number of moles in a gas mixture, n_{total}, according to Dalton's law of partial pressures

$$P_B = X_B P_{total} \tag{2.38}$$

where P_{total} is the total pressure of the mixture of gases [31].

Henry's Law Constant, H, is denoted as (1/Solubility), which is described by (2.30) and (2.31). From the ideal gas law,

$$PV = n\mathrm{R}T \tag{2.39}$$

and Dalton's law of partial pressures the concentration (g of gas/m^3 of air) of substance, C_A, in the air phase is a function of its partial pressure

$$C_A = \frac{wn_B}{V} = \frac{wP_B}{RT} \tag{2.40}$$

where w, is the molecular weight of the gas, n_B is the number of moles in a gas mixture of volume, V. Combining (2.30) and (2.40) yields

$$C_A = \frac{wP_B}{RT} = \frac{wH}{RT}C_P = wK_{AP}C_P \tag{2.41}$$

where C_P is the concentration (g of gas/m^3 of polymer) of the chemical substance in the polymer and K_{AP} is the dimensionless thermodynamic partition coefficient of the air-polymer interface. The relationship of C_A versus C_P is usually linear with a slope of K_{AP}. The limits of these concentration values are determined by the maximum concentration of the chemical substance in the air phase, C^S_A, which is derived from (2.40), and the maximum achievable concentration (g of gas/m^3 of polymer) of the chemical species in the polymer, C^S_P. C^S_P is derived from, c, the volume concentration (cm^3 of gas/cm^3 of polymer) in (2.30)

$$C_P^S = c\rho_{\text{gas}} \cdot \frac{10^6 \text{cm}^3}{\text{m}^3} \tag{2.42}$$

where ρ_{gas} is the density (g/cm^3) of the gas. Figure 2.6 illustrates (2.41) and these maximum concentration limits [32]

FIGURE 2.6 *Thermodynamic partition coefficient, K_{AP} (extracted from [32])*

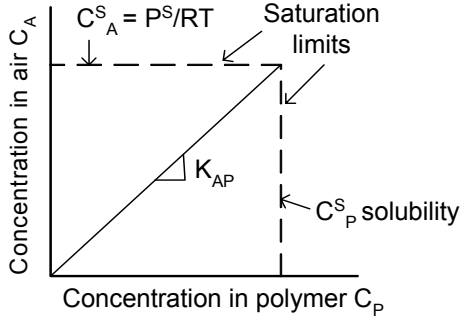

where P^S is the vapor pressure of the chemical species. The particular analyte polymer partition coefficient may be estimated by comparing the maximum concentration of the analyte in air versus the solubility of the analyte in the polymer medium as shown in the following

$$\text{K}_{\text{AP}} = \left(\frac{\text{C}_A^S}{\text{C}_P^S}\right) = \left(\frac{1}{\text{K}_{\text{PA}}}\right) \tag{2.43}$$

$$\text{K}_{\text{PA}} = \left(\frac{\text{RT}}{w\text{P}^S}\right) c\rho_{\text{gas}} \cdot \frac{10^6 \text{cm}^3}{\text{m}^3} \tag{2.44}$$

Combining (2.30), (2.37), and (2.44) with the values listed in Table 2.1, the partition coefficients of particular gas chemicals pertinent to this work in a

partially crystalline polystyrene medium may be calculated. Table 2.2 summarizes these values.

TABLE 2.2 *Partition coefficients for gas chemicals in polystyrene (STP) and the densities and molecular weights of these materials*

Chemical Substance	K_{PA} (m^3 of air/m^3 of polymer)	density (g/cm^3)	molecular weight (g/mol)
methanol	34,681	0.7914	32.04
ethanol	35,447	0.7893	46.07
2-propanol	30,296	0.7855	60.10
acetone	14,970	0.7899	58.08
water	208,850	1.0	18
polystyrene (n = 1)		0.9060	104.15

2.3 Total System

In order to predict a resonant frequency shift per concentration of the gas chemical, several factors must be considered: concentration of the drop of polystyrene cast in solution, the volume of a drop deposited from the ink jet system, the density of polystyrene as well as the gas chemical being absorbed, and the thermodynamic partition coefficient. The potential mass shift per drop of polystyrene cast in solution as a function of concentration (g/m^3) of the gas chemical concentration, C_B, in the surrounding environment is described by

$$\frac{\Delta m}{drop} = C_B \frac{\left(\frac{4}{3}\pi R_{drop}^3 C_{drop}\right)}{\rho_{poly}} \left(\frac{1}{K_{AP}}\right) \tag{2.45}$$

$$\frac{\Delta m}{drop} = C_B \frac{\left(\frac{4}{3}\pi R_{drop}^3 C_{drop}\right)}{\rho_{poly}} \left(\frac{C_P}{C_G}\right) \tag{2.46}$$

where R_{drop} is the radius of the drop, C_{drop} is the concentration of the polystyrene (g/mL) in solution that is ink jetted onto the gravimetric device, C_P the mass concentration of analyte in the polymer (g/cm^3), C_G the mass concentration of the analyte in the air (g/cm^3), and the ρ_{poly} the density (g/cm^3) of the polystyrene.

2.3.1 Cantilever Gravimetric Sensitivity

The cantilever concentration sensitivity, *J*, [4]

$$J = \frac{\Delta f_o}{\Delta c_B} \tag{2.47}$$

describes the change in frequency per change in analyte gas concentration. By combining (2.8) and (2.45) the concentration sensitivity per drop of polystyrene becomes

$$J = \frac{\Delta f_o}{\Delta m} \cdot \frac{\Delta m}{\Delta c_B} \tag{2.48}$$

$$J = -\frac{f_o}{2(m_o + m_{polystyrene})} \frac{\left(\frac{4}{3}\pi R_{drop}^3 C_{drop}\right)}{\rho_{poly}} \left(\frac{1}{K_{AP}}\right) \tag{2.49}$$

where m_o is the mass of the cantilever without polystyrene and $m_{polystyrene}$ is the mass of polystyrene placed onto the end plate of the resonator. Equation 2.49 illustrates that in order to increase the device sensitivity to gas concentration, the device mass should be as small as possible. The concentration of the drop C_{drop} may be increased, but has a maximum limit determined by the ink jet nozzle, i.e. higher concentration drops tend to clog the ink jet nozzle. This may be alleviated simply by increasing the number of drops deposited onto the device. The number of drops deposited may be increased, but there is a maximum limit of the amount of polymer that may be deposited. This limit is determined by the finite dimensions of the drop platform. By including the added mass of the sensitive layer in the device sensitivity, from (2.7), the resulting sensitivity may be evaluated in the following

$$J = -\frac{1}{4\pi} \frac{\sqrt{k}}{\sqrt{\left(m_o + \frac{4}{3}\pi R_{drop}^3 C_{drop} N_{drop}\right)^3}} \left(\frac{4}{3}\pi R_{drop}^3 C_{drop} N_{drop}\right) \left(\frac{1}{K_{AP}}\right) \left(\frac{1}{\rho_{poly}}\right) \tag{2.50}$$

The sensitivity increases with added quantities of polymer up until a certain point where the following derivative

$$\frac{dJ}{dN_{\text{drop}}} = \frac{\sqrt{k}}{4\pi}\left(\frac{1}{K_{AP}\rho_{\text{poly}}}\right)\left(-\frac{1}{\sqrt[3]{\left(m_o + \frac{4}{3}\pi R_{\text{drop}}^3 C_{\text{drop}} N_{\text{drop}}\right)}} + \frac{\frac{3}{2}\left(\frac{4}{3}\pi R_{\text{drop}}^3 C_{\text{drop}} N_{\text{drop}}\right)}{\sqrt[5]{\left(m_o + \frac{4}{3}\pi R_{\text{drop}}^3 C_{\text{drop}} N_{\text{drop}}\right)}}\right) \quad (2.51)$$

is equal to 0. At this point the sensitivity is negatively affected by the mass of the polymer placed on the device. This occurs when

$$N_{\text{drop}} = \frac{3m_o}{2\pi R_{\text{drop}}^3 C_{\text{drop}}} \quad (2.52)$$

or when

$$m_{polystyrene} = 2m_o \quad (2.53)$$

where $m_{\text{polystyrene}}$ is the mass of the polystyrene. At this point the amount of polystyrene deposited exceeds the volume of the platform in which the polymer is contained. Therefore, increasing the maximum number of allowable drops is advantageous and provides a higher chemical sensitivity (Hz/ppm). The maximum sensitivity that may be achieved using (2.50) and (2.53) is

$$J = -\frac{f_o}{3^{1.5}}\left(\frac{1}{K_{AP}\rho_{\text{poly}}}\right) \quad (2.54)$$

2.3.2 Minimum Detectable Concentration

The device concentration resolution limit is

$$(\Delta c_B)_{\min} = \frac{\Delta c_B}{\Delta m}(\Delta m)_{\min} \quad (2.55)$$

By combining (2.24) and (2.55) the minimum detectable concentration is

$$(\Delta c_B)_{\min} = \left(m_o + \frac{4}{3}\pi \mathrm{R}_{\mathrm{drop}}^3 \mathrm{C}_{\mathrm{drop}} N_{\mathrm{drop}}\right) \frac{1}{X_o} \sqrt{\frac{k_B T f_{BW}}{f_o k Q}} \left(\frac{6 K_{AP} \rho_{\mathrm{poly}}}{\pi \mathrm{R}_{\mathrm{drop}}^3 \mathrm{C}_{\mathrm{drop}} N_{\mathrm{drop}}}\right) \quad (2.56)$$

Using the amount of polystyrene to achieve the highest concentration sensitivity derived in (2.53) the minimum detectable concentration evaluates to be

$$(\Delta c_B)_{\min} = \frac{12}{X_o} \sqrt{\frac{k_B T f_{BW}}{f_o k Q}} (K_{AP} \rho_{\mathrm{poly}}) . \quad (2.57)$$

Using the experimental values of f_{BW} = 1Hz, k = 0.298 N/m, f_o = 5.8 kHz, Q = 56, T = 298 K, X_o of 90 nm, k_B = 1.38 x 10^{-23} J/K, a calculated K_{AP} = 1/34,681 = 2.88 x 10^{-5}, and ρ_{poly} = 0.906 g/cm^3 the minimum detectable concentration evaluates to be 6.92 x 10^{-10} g/cm^3. Converting this to units of ppm we get

$$(\Delta c_B)_{\min}(\mathrm{ppm}) = \left((\Delta c_B)_{\min}\left(\mathrm{in}\frac{\mathrm{g}}{\mathrm{cm}^3}\right)\right) \cdot \frac{1}{w} \cdot \frac{RT}{P} \cdot \frac{10^6 \mathrm{cm}^3}{\mathrm{m}^3} \cdot 10^6 \quad (2.58)$$

$$(\Delta c_B)_{\min}(\mathrm{ppm}) = \frac{6.92 \cdot 10^{-10} \mathrm{g}}{\mathrm{cm}^3} \cdot \frac{\mathrm{mol}}{32 \mathrm{g}} \cdot \frac{8.314 \mathrm{Pa} \cdot \mathrm{m}^3}{\mathrm{mol} \cdot \mathrm{K}} \cdot \frac{298 \mathrm{K}}{10^5 \mathrm{Pa}} \frac{10^6 \mathrm{cm}^3}{\mathrm{m}^3} \cdot 10^6 \quad (2.59)$$

to yield the minimum detectable concentration of 0.535 ppm. This corresponds to an optimal sensitivity of - 0.058 Hz/ppm using (2.54). For the current work the device tested had 31 drops of 2mg/mL of polystyrene in solution. Using (2.50), (2.56), m_o = 65 ng, R_{drop} = 20 μm, the current device has a sensitivity of - 0.0081 Hz/ppm and a minimum detectable methanol con-

centration of 6.5 ppm. Table 2.3 shows the calculated sensitivity and the cal-

TABLE 2.3 Calculated sensitivity and minimum detectable concentration of the current device based on 31 drops of polystyrene in 2mg/mL solution

Chemical Substance	Calculated Sensitivity (Hz/ppm)	Calculated minimum detectable concentration (ppm)
methanol	-0.0081	6.5
ethanol	-0.012	4.4
2-propanol	-0.0133	4.0
acetone	-0.0064	8.3

culated minimum detectable concentrations of the current device based on 31 drops of polystyrene in 2mg/mL solution for each particular analyte.

2.4 Electrostatic Actuation

In the current work, actuation and sensing were implemented using electrostatic comb drives. The transduction from the electrical domain into the mechanical domain may be described by the two-port capacitor model where the controlling input is voltage and the output is force.

The equation for a parallel plate capacitor is defined by

FIGURE 2.7 *Two Port Capacitor Model*

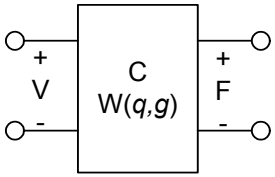

$$q = CV, \tag{2.60}$$

where q is the charge on the capacitor with capacitance

$$C = \frac{\varepsilon A}{g}, \tag{2.61}$$

where g is the gas distance between the capacitor electrodes, A is the area of the capacitor electrodes, and ε the dielectric constant of air. The energy, W, stored in a capacitor with an applied voltage, V, is

$$W = \frac{1}{2}CV^2 \tag{2.62}$$

$$W = \frac{\varepsilon A}{2g}V^2. \tag{2.63}$$

Consequently, the electrostatic force induced by an applied voltage, V, across a capacitor is the derivative of the energy stored with respect to the gap, i.e.

$$F = -\frac{dW}{dA}\bigg|_{V,h} \tag{2.64}$$

where $A = xh$. The direction of motion, x, is defined in Figure 2.1 and h is the height of the comb finger electrodes. In the comb drive electrodes, g is considered constant to the first order. The force evaluates to

$$F_{electrostatic} = \frac{1}{2}\left(\frac{dC}{dx}\right)V^2 \tag{2.65}$$

Electrostatic actuation for this device is intended to be parallel to the surface of the silicon substrate. An advantage of utilizing the comb drive is that the $\frac{dC}{dx}$ is constant as long as the displacement x does not exceed the overlap of the fingers in the drive. The voltage in (2.65) represents the potential difference between the driving comb electrodes and that of the cantilever. Figure 2.1 shows that there are two comb drive electrodes, one on either side of the cantilever, and, consequently, two forces acting upon the cantilever. The potential difference between the left drive and the cantilever and the difference between the right drive and the cantilever are

$$V_{Lc} = V_{Left} - V_b \tag{2.66}$$

$$V_{Rc} = V_{Right} - V_b \tag{2.67}$$

The net electrostatic force, F_{ext}, acting on the cantilever is the difference between the two forces from the left and right comb drives

$$F_{ext} = \frac{1}{2}\left(\frac{dC}{dx}\right)(V_{Lc}^2 - V_{Rc}^2). \quad (2.68)$$

Combining (2.66), (2.67), and (2.68) yields the total external force acting on the cantilever

$$F_{ext} = \frac{1}{2}\left(\frac{dC}{dx}\right)(V^2{}_{Left} - 2V_{Left}V_b + 2V_{Right}V_b - V_{Right}^2) \quad . \quad (2.69)$$

For this work $V_{Right} = V_R\cos(\omega_R t)$, V_b is a DC voltage, and V_{Left} = 0 V. Equation 2.69 simplifies to

$$F_{ext} = \frac{1}{2}\left(\frac{dC}{dx}\right)(2V_bV_R\cos(\omega_R t) - V_R^2(\cos\omega_R t)^2) \quad (2.70)$$

$$F_{ext} = \frac{1}{2}\left(\frac{dC}{dx}\right)\left(2V_bV_R\cos(\omega_R t) - \frac{V_R^2}{2} - \frac{V_R^2}{2}\cos(2\omega_R t)\right) \quad . \quad (2.71)$$

Electrostatic force components exist at ω_R, $2\omega_R$, and DC.

2.5 Differential Capacitive Sensing

The current through the capacitor is found by taking the derivative of the charge on the capacitor, Equation 2.60, is

$$I = C\left(\frac{dV}{dt}\right) + V\left(\frac{dC}{dt}\right) \quad (2.72)$$

Taking the Laplace transform of the current through the capacitor yields the following

$$I(s) = C \cdot sV(s) + V \cdot sC(s) \tag{2.73}$$

Interdigitated comb drives are used for capacitive sensing of motion. The current induced by the motion of the resonator is described by

$$I = V_b\left(\frac{dC}{dx}\right)\left(\frac{dx}{dt}\right) \tag{2.74}$$

where V_b is the bias voltage between the resonator and the sensing comb drives that are placed on either side of the resonator structure. The Laplace transform of (2.74) and the resulting current-displacement transfer function using (2.3) for $x(s)$ is as follows

$$I(s) = sV_b\left(\frac{dC}{dx}\right)\frac{F_{ext}(s)}{ms^2 + Bs + k} \tag{2.75}$$

Combining (2.75) with the net force on the resonator from (2.69) the motional current signal at one of the inputs of the differential amplifier results in the following

$$I(s) = sV_b\frac{1}{2}\left(\frac{dC}{dx}\right)^2\frac{(V_{ext}(s) - V_b)^2}{ms^2 + Bs + k} \tag{2.76}$$

The total current signal includes drive signal feed through via parasitic capacitances, C_p, to the pre-amplifier.

$$I_{TOTAL}(s) = C_p \cdot sV_{ext}(s) + sV_b\frac{1}{2}\left(\frac{dC}{dx}\right)^2\frac{(V_{ext}(s) - V_b)^2}{ms^2 + Bs + k} \tag{2.77}$$

The resonator position transduction into the electrical domain is implemented by capacitive detection using an on-chip amplifier. This circuit outputs a voltage proportional to the difference of the current through the comb finger capacitors placed on either side of the resonator. As the area of the comb drive changes there is a capacitance increase on one side and a corresponding decrease on the opposing side of the resonator.

This capacitance change is related to the change in the current in the two inputs of the differential amplifier. The on-chip preamplifier is a differential voltage amplifier described in [23]. The gain, G, and bandwidth are 137 and 10.5 MHz, respectively. Figure 2.8 illustrates the circuit and device sizings (in microns) of the preamplifier which was designed by Brotz [24].

2.5.1 Resonator and Pre-amplifier Analysis

From (2.74) the current-displacement transfer function is as follows

$$\frac{I(s)}{x(s)} = sV_b\frac{dC}{dx} \tag{2.78}$$

The pre-amplifier is a voltage amplifier and Figure 2.9 illustrates the input capacitance associated with its model and the voltage, V_c, is

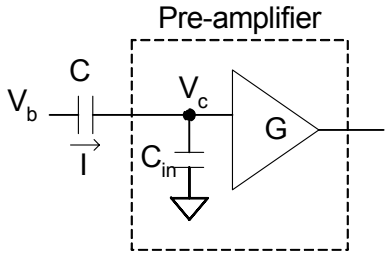

FIGURE 2.9 *On chip pre-amplifier*

FIGURE 2.8 *On Chip Preamp and Bias Circuit Sizing by Brotz [24]*

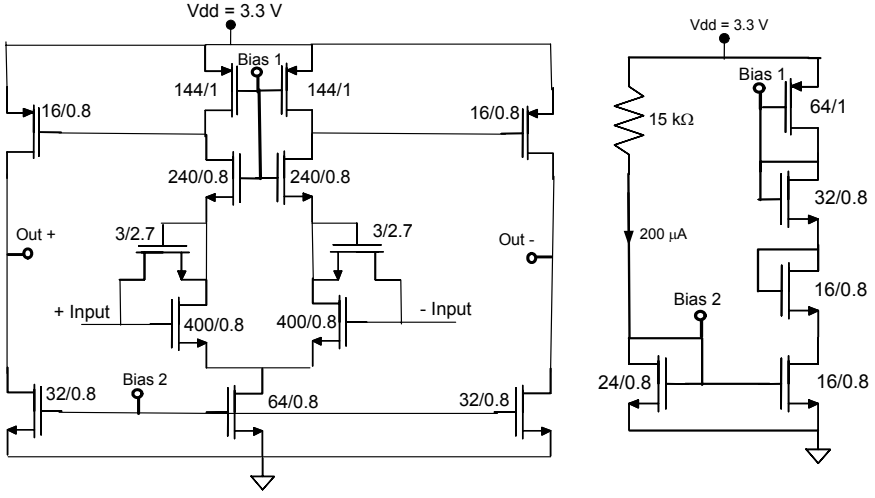

$$V_c(s) = \frac{I(s)}{sC_{in}} \tag{2.79}$$

Combining (2.78) and (2.79) yields

$$\frac{V_c(s)}{x(s)} = \frac{V_b}{C_{in}} \cdot \frac{dC}{dx} \tag{2.80}$$

Since the resonance frequency of interest, ~ 5 kHz, is well below the roll-off frequency of the pre-amplifier, 10 MHz, the pre-amplifier has approximately 0 ° phase shift at 5kHz with a gain, G = 137. The transfer function and voltage output of the pre-amplifier, based on the resonator motional current, is

$$V_{out}(s) = \frac{G}{C_{in}} V_b \frac{dC}{dx} \frac{1}{ms^2 + Bs + k} \tag{2.81}$$

$$V_{out}(s) = \frac{G}{C_{in}} V_b \left(\frac{dC}{dx}\right)^2 \frac{(V_{ext}(s) - V_b)^2}{ms^2 + Bs + k} \tag{2.82}$$

Since the input into the pre-amplifier is differential, (2.81) only shows the output as a function of a non-differential motional current input and, therefore, there is a factor of 2 missing. The output including a differential input and parasitics is

$$V_{out}(s) = \frac{2G}{C_{in}} \left(C_p \cdot V_{ext}(s) + V_b \frac{1}{2} \left(\frac{dC}{dx}\right)^2 \frac{(V_{ext}(s) - V_b)^2}{ms^2 + Bs + k} \right). \tag{2.83}$$

The pre-amplifier provides 0° phase shift from DC to 1 MHz. At DC the open loop phase shift of the resonator and pre-amplifier is 0° and the resonator provides a total of 180° phase shift. At the resonant frequency the phase the phase of the open loop system is 90°.

2.6 Mass Sensitive Oscillator

A perturbation from the outside environment, such as a change in the concentration of the environment surrounding the resonator, induces a shift in the resonant frequency of the system. An important feature of a mass sensor is to continuously track its resonant frequency in response to these perturbations. This implies the utilization of the resonator in oscillation mode where the external circuitry provides proper gain and phase compensation to track the resonance frequency of the device.

In order to achieve oscillation in a feedback systems, it is important that the gain be greater than one and that the total phase shift of the entire loop is 0° or multiples of 360° at the desired frequency of oscillation. This is known as the Barkhausen criteria for the system loop transfer function, $T(s)$ [21].

Figure 2.10 shows feedback schemes where the total phase shift of the entire loop is equal to either 0° or 360° degrees at the oscillation frequency of interest $s = j\omega_r$. The signal generated around the loop at the frequency of interest should add in phase with this initial signal. The oscillating frequency is a frequency component of the thermal noise in the loop that satisfies the Barkhausen criteria. As the signal travels around the loop, the signal regener-

FIGURE 2.10 *Feedback Schemes to Achieve Oscillation*

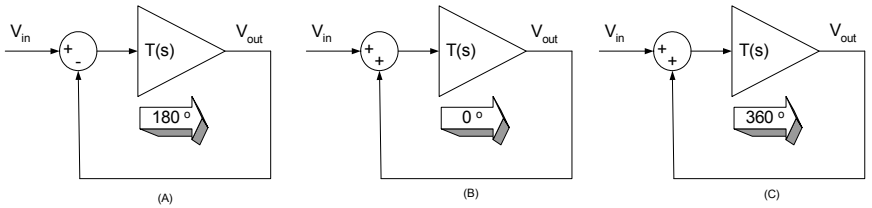

ates itself with a greater magnitude after each successive iteration so at the frequency of interest a growing oscillation occurs. Eventually, saturation voltages will be reached. These voltages may be determined by output voltage swing limits of the amplifiers used in the oscillation scheme or explicit limiting electronics may be inserted into the loop. In this work, the swing is limited by the supply and bias voltages of the amplifiers.

For the chemical mass sensitive device in the current work, the oscillation frequency of interest is the natural resonator frequency. Since the phase shift of the resonator is -90 ^{o} at resonance, an external phase compensation circuit is needed in order to achieve both the total phase and gain criteria. The exact compensation from this external circuitry is discussed next.

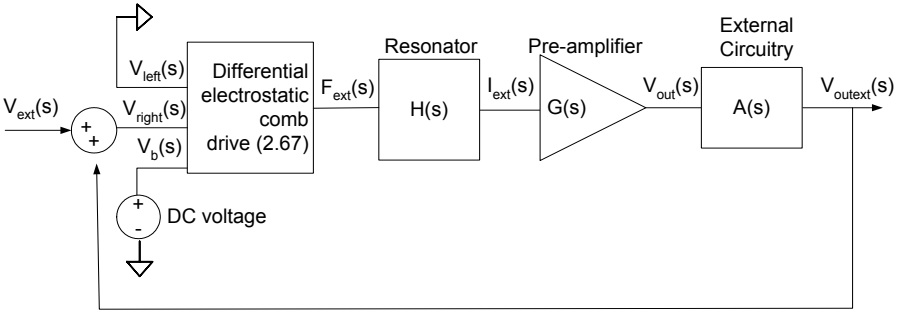

FIGURE 2.11 *Oscillation Loop*

2.7 Oscillator Loop

Figure 2.11 shows the total system in feedback condition where *H(s)* represents the mechanical resonator, *U(s)* the on-chip pre-amplifier, and *A(s)* the off-chip phase compensation circuit transfer functions. The loop gain of the system is

$$T(s) = H(s)U(s)A(s) \tag{2.84}$$

Figure 2.12 illustrates the phase of the resonator cascaded with the on-chip pre-amplifier, $H(s)U(s)$. To achieve a total loop phase shift of 0°, external electronics are needed to provide a phase compensation of -90° and a gain greater than unity at the resonant frequency.

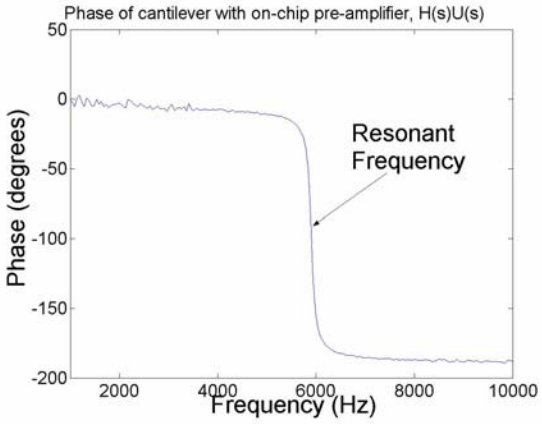

FIGURE 2.12 *Measured phase of cantilever cascaded with on chip pre-amplifier*

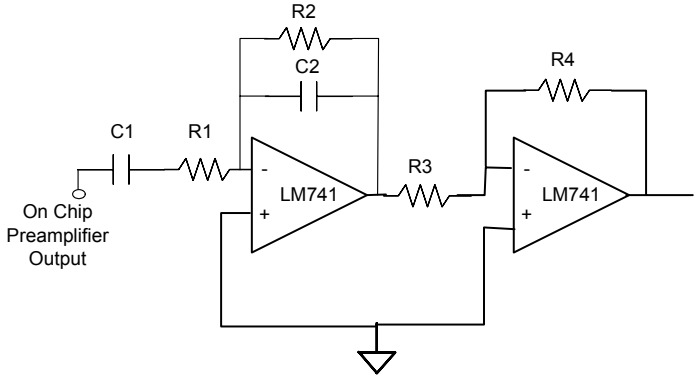

FIGURE 2.13 *External Circuit*

2.7.1 External Circuit Analysis

The external circuit in Figure 2.13 provides additional gain and phase to the oscillator loop. Two inverting off-chip stages are utilized; one for phase

compensation and the other for additional gain. The total response of the off-chip circuitry is non-inverting with transfer function

$$A(s) = \frac{R_4}{R_3}\frac{sC_1R_2}{(1+R_2C_2s)(1+R_1C_1s)} \tag{2.85}$$

The pole frequencies are chosen at frequencies one decade less than the resonant frequency so that at resonant frequency the total phase shift in the loop is 360°. LM741 op-amps with a gain-bandwidth product of 1 MHz are adequate since the resonance frequency of the resonator is 5.6 kHz. The off chip amplifier has a zero at DC and two poles at

$$p_1 = \frac{1}{2\pi R_1C_1} \tag{2.86}$$

$$p_2 = \frac{1}{2\pi R_2C_2} \tag{2.87}$$

For oscillation at 5.6 kHz, we chose $R_1 = 10\ \Omega$, $R_2 = 3\ k\Omega$, $R_3 = 1\ k\Omega$, $R_4 = 100\ k\Omega$, $C_1 = 100\ \mu F$, and $C_2 = 0.1\ \mu F$. A plot of the transfer function (magnitude and phase) is given in Figure 2.14. At resonant frequency, the magnitude and phase are 70 dB and -84°, respectively. The loop gain of the sytem becomes

$$\frac{V_{outext}(s)}{F_{ext}(s)} = L(s) = s2G\frac{V_b}{C_{in}}\cdot\frac{dC}{dx}\cdot\frac{1}{ms^2+Bs+k}\left(\frac{R_4}{R_3}\frac{C_1R_2}{(1+R_2C_2s)(1+R_1C_1s)}\right) \tag{2.88}$$

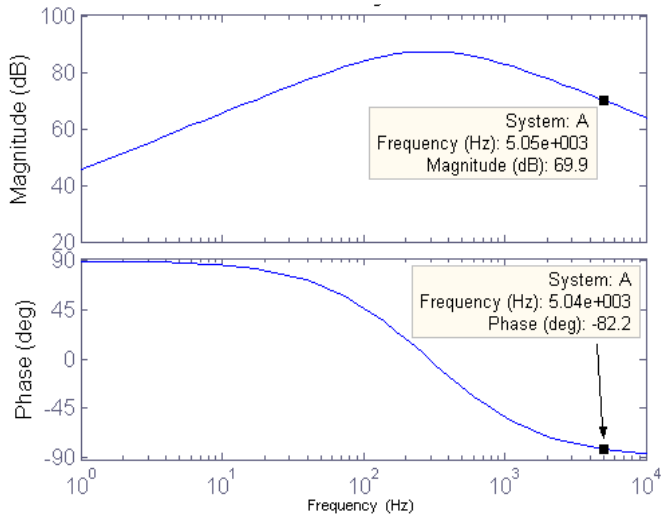

FIGURE 2.14 *External Circuit Magnitude and Phase*

$$\frac{dC}{dx} = \frac{2N\varepsilon_o h}{g_o} \tag{2.89}$$

where $V_{outext}(s)$ is the output voltage of the external circuit, N is the number of fingers, ε_o is the permittivity of free space, h is the height of the comb finger electrodes, and g_o is the gap between the fingers. Using the pre-amp gain, G = 137, V_b = 20 V, N = 7, ε_o = 8.85 x 10^{-12} F/m, h = 1.905 µm, g_o = 1.0 µm, C_{in} = 0.5 fF, m = 2.51 x 10^{-10} kg, k = 0.298 N/m, and Q = 56 (which was experimentally determined) the magnitude and phase of the loop gain, based on the motional current, is illustrated in Figure 2.15. The magnitude and phase at resonance are 300 dB and ~ -180°, respectively. To change the phase from -

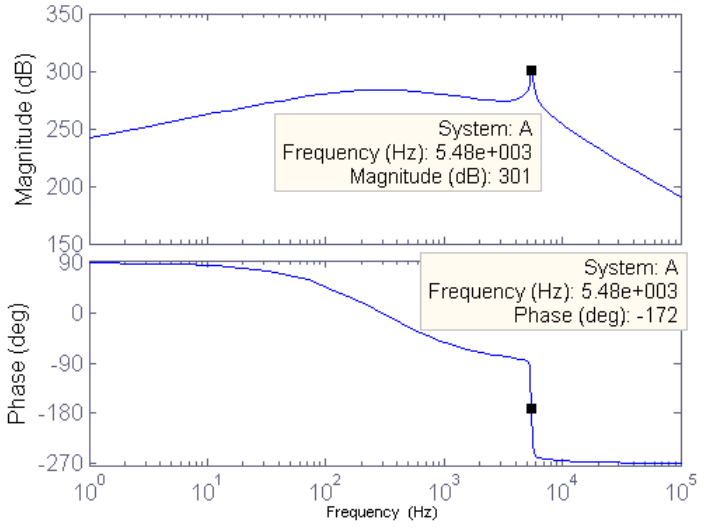

FIGURE 2.15 *Loop Gain Magnitude and Phase*

180° to 0° the amplifier in the second stage of the external circuit shown in Figure 2.13 may be switched from an inverting configuration to a non-inverting one.

Evaluating the loop gain with the drive signal feed through to the preamplifier from parasitic capacitances using (2.77), (2.79), and (2.85) the output of the three stages, $V_{outext}(s)$, evaluates to

$$V_{outext}(s) = s2\frac{G}{C_{in}}\left(C_p \cdot V_{ext}(s) + V_b\frac{1}{2}\left(\frac{dC}{dx}\right)^2\frac{(V_{ext}(s)-V_b)^2}{ms^2+Bs+k}\right)\left(\frac{R_4}{R_3}\frac{C_1R_2}{(1+R_2C_2s)(1+R_1C_1s)}\right) \quad (2.90)$$

With the drive signal feed through the actual signal magnitude may higher than magnitude induced by the motional current. If this occurs one would not be able to detect the resonant frequency of the cantilever.

3 Design and Experiment

3.1 Design Considerations

The MEMS gravimetric device was designed in the CMOS MEMS technology which allows for direct integration with CMOS electronics. During the course of the research two generations of devices were designed, fabricated, post-processed, and the subsequent gravimetric sensors were tested for gas sensitivity. The following presents the successful second generation design and implementation. Future work will address full optimization for maximum gas sensitivity in this technology.

There are design limitations and considerations to be addressed in this technology. There are also issues concerning the ink-jet printing process used for receptor chemistry deposition. For device layout considerations the following characteristics are desired of the MEMS structure.

1. The resonator should have a dominant resonance mode at the operating frequency at which oscillation occurs.

2. Lateral (in-plane) operation of the device must be implemented to maintain linearity in the comb-finger drive operation.

3. Drive signal feedthrough, from parasitic capacitances, should be minimized through careful placement of electrodes, as well as the use of electrical shielding.

4. The resonator area and ink-jet deposition spot size must be compatible.

5. The ink-jet drop target of the resonator structure should be placed far enough away from other mechanical structures so that polymer bridging and "gluing" does not occur between the structures. Such bridging would inhibit actuation.

The CMOS MEMS technology places limits on the device sizes and materials that can be used. The mechanical structures are implemented through metal and silicon dioxide stacks. The height of this stack is limited by the number of metal layers utilized in the particular process. The minimum gap between mechanical structures is determined by the foundry and by the post-CMOS

processing conditions necessary for release of the MEMS structure from the substrate.

A simple mechanical design was chosen, consisting of a cantilever beam with the free end attached to a plate, used as a polymer drop target. The plate included a stiffening rim with a 6 μm height. The width of the beam was sized to be smaller than its height to keep the vertical resonance out of the range of the lateral resonance mode. Figure 3.1 shows an SEM of the first iteration of the gravimetric design implemented using the TSMC four metal 0.35 μm CMOS process.

FIGURE 3.1 *Resonator design #1 with cross-section of target end plate for polymer*

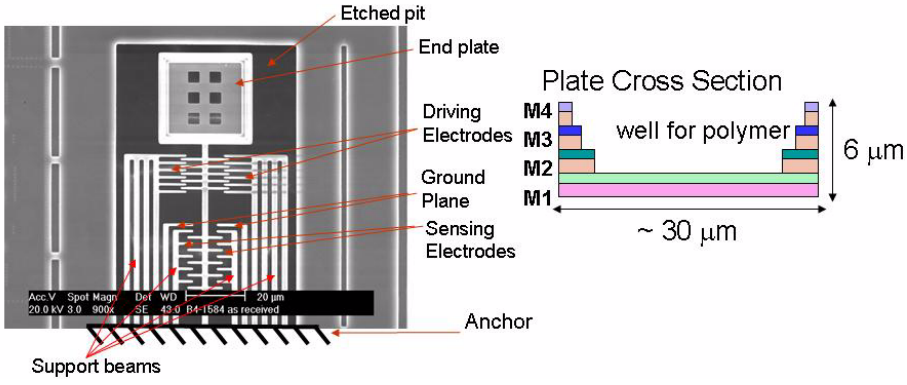

Residual stresses due to process conditions at the foundry commonly induce curling in long cantilever structures. Actuating and sensing electrodes must compensate for this phenomenon. To compensate for vertical curling of the structures the widths of the driving and sensing electrode support beams are identical to the resonator beam width. Stiffening ribs were added to the driving electrodes to keep the resonant frequency of this stator structure out of the range of the gravimetric structure's primary resonant frequency. A ground shield was placed between the drive and sensing electrodes and connected to the substrate, which is set to the lowest voltage in the system. This shield should minimize the feedthrough of the actuating potentials to the sensing circuit. There were two major design issues learned from this first prototype. First, stiffening ribs should be added to the sensing electrodes to ensure that its resonant frequency is out of the range of the beam and end plate resonant frequency. Second, the target plate should be larger to accommodate the ink-jet drop dimensions.

Figure 3.2 shows the resulting polymer that was jetted onto the MEMS structure. The left SEM view of the gravimetric structure reveals a polymer bridge between the end plate and the outer structural support. The other image shows polymer bridging between sensing electrodes and the beam. These

FIGURE 3.2 *Bridging of polystyrene (10 drops of 1 mg/mL) on the gravimetric device to the supporting rim and electrode fingers*

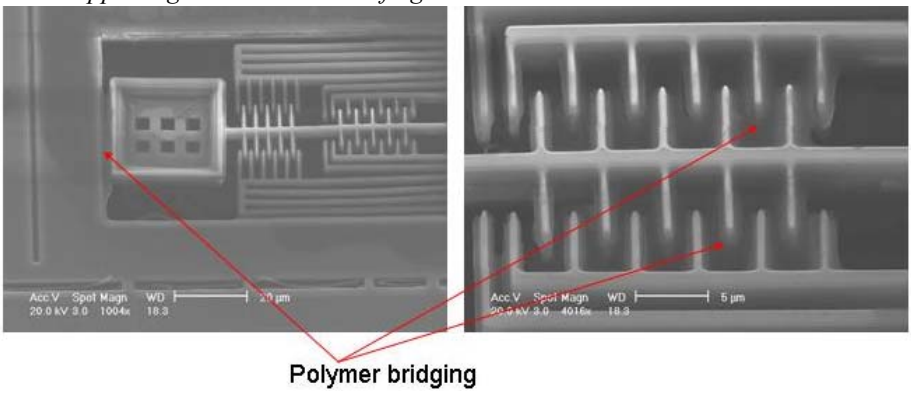

bridges glue the movable structure to the fixed structures and inhibit the actuation and motion, rendering the device inoperable.

The SEM in Figure 3.3 shows the second-generation design using the Jazz 0.35 μm BiCMOS process. For this design, stiffening ribs were added to the ground shield electrode as well as to the sensing electrodes. The volume of the end plate was sized to accommodate an approximately 30-50 μm diameter drop emitted from the ink-jet. The drop volume ranges between 14 and 65 pL. The volume of the end plate inner width, inner length, and rim height were sized to be 109.9 μm, 96.8 μm, and 7.98 μm, respectively, and corresponds to an approximate volume of 85 pL. The outer rim placed along the edges of the plate has a width of 3.2 μm, so the total plate dimension is 116.4 μm by 103.2

FIGURE 3.3 *Second-generation resonator design*

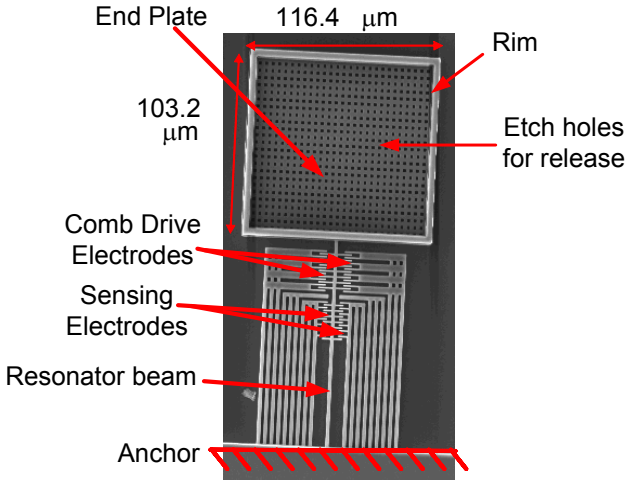

μm. A typical drop contains approximately 3.5 fL of polystyrene. Therefore, the end plate volume could hold a maximum equivalent amount of polystyrene that would be cast from approximately 1500 drops of solvent/polymer solution. Figure 3.4 is a digital image of two identical devices. The device on he left shows the result of two drops of polythiophene in a 1mg/mL 1 toluene:1 xylene solution. The device on the right has one drop. The volume of the end plate successfully accommodates the drop which includes both solvent and polymer.

FIGURE 3.4 *Polythiophene (1 mg/mL 1toluene:1xylene) drops on two identical devices. Left and right devices have 2 and 1 drops, respectively.*

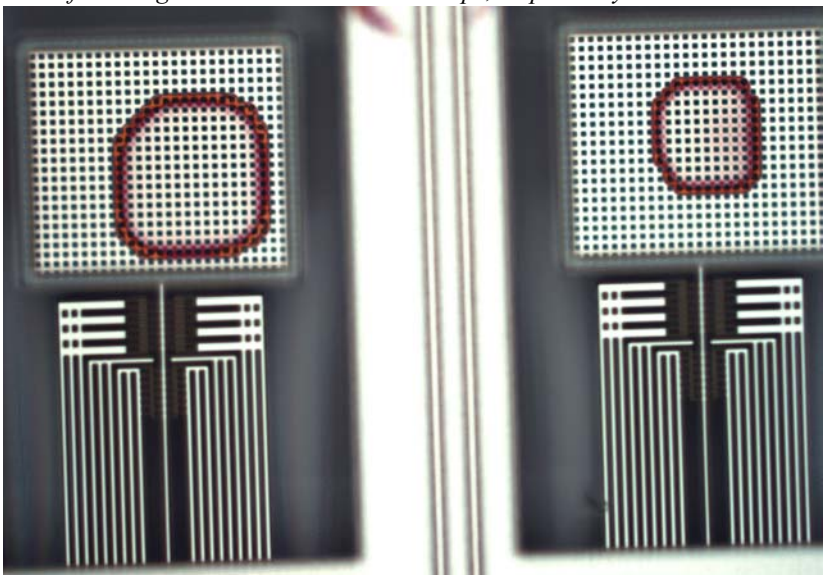

3.2 Drop Tests and System Response

Based on Equation 2.50 the sensitivity to ethanol versus the number of drops deposited on the Jazz device is plotted in Figure 3.5 The peak in sensitivity occurs at 21,140 drops, which corresponds to a polymer volume of 74 pL. This exceeds the volume of the plate by two orders of magnitude, so this is not possible with the given design. However, the maximum amount of polymer that is physically possible to fit on the drop plate should be deposited.

FIGURE 3.5 *Sensitivity to ethanol vs. number of drops of polystyrene*

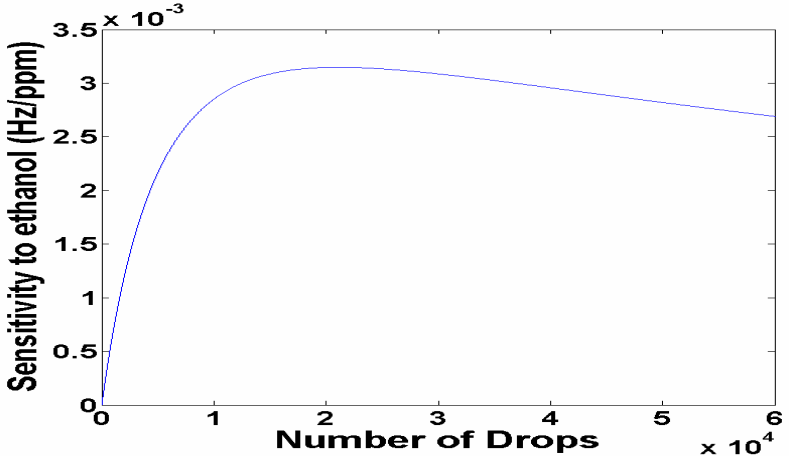

There were several chips tested for the current work, labelled 2_10_j2, 12_12_j3, 5_13_j1, and 2_10_j4. No polystyrene was deposited on 12_12_j3 as this gravimetric device served as a control. The gravimetric device on the 2_10_j2 chip had 31 total drops of polystyrene cast from a 2 mg/mL 1 toluene:1 xylene solution. To ensure that the polymer well (drop plate) did not overflow from all of the solvent sufficient drying time was allowed between the deposited drops. A conservative approach was taken, i.e. only a few drops were deposited at a time with several second delay between the groups of drops. Table 3.1 through Table 3.3 document the jetting conditions this for

three separate devices. Between each drop iteration there was approximately 5 minutes delay time.

TABLE 3.1 *Drop experiment protocol for device on 2_10_j2 chip (31 drops total). The iteration numbers are in chronological order. The time between iterations is approximately 5 minutes.*

Iteration number	Number of drops	Delay between drops (sec)
1	3	1
2	3	1
3	3	1
4	3	1
5	3	1
6	6	5
7	10	5
total	total = 31	

TABLE 3.2 *Drop experiment protocol for device on 2_10_j4 chip (90 drops total)*

Iteration number	Number of drops	Delay between drops (sec)
1	5	10
2	5	10
3	5	10
4	5	10
5	10	10
6	10	10
7	10	10

TABLE 3.2 *Drop experiment protocol for device on 2_10_j4 chip (90 drops total)*

8	10	10
9	10	10
10	10	10
11	10	10
total	90	

TABLE 3.3 *Drop experiment protocol for device on 5_13_j1 chip (57 drops total)*

Iteration number	Number of drops	Delay between drops (sec)
1	2	10
2	5	10
3	5	10
4	5	10
5	5	10
6	5	10
7	10	10
8	10	10
9	10	10
total	57	

FIGURE 3.6 *Digital image of 57 drops of polystyrene on 5_13_j1 chip (left), 90 drops on 2_10_j4 chip (center), and 31 drops on 2_10_j2 chip (right)*

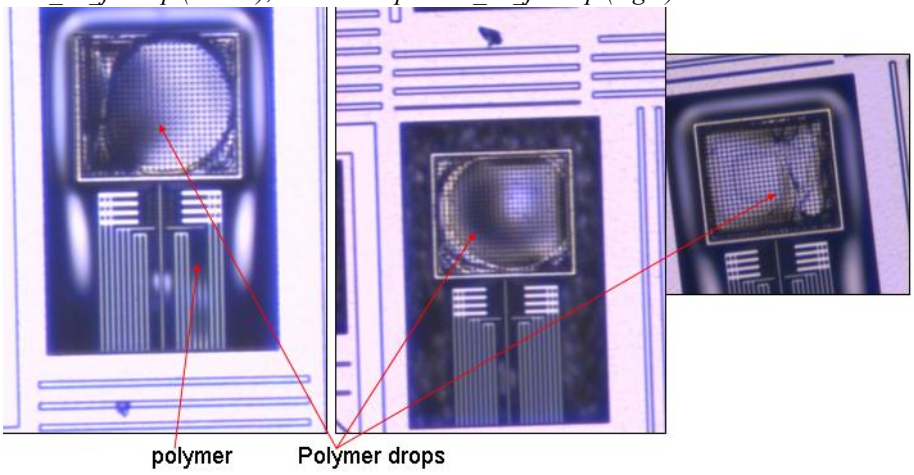

Figure 3.6 shows the digital images of polystyrene deposited on the three gravimetric devices. The devices with 57 drops (5_13_j1 chip) and 90 drops (2_10_j4 chip) of polystyrene could not be actuated after the drops were deposited and dried. The volume of the polystyrene polymer for these numbers of drops are calculated to be 4.2 and 6.7 pL, respectively. These volumes are both smaller than the volume of the target drop plate. There is no visible bridging between the fingers on either of the devices. However, there is some polymer on the stiffening ribs of the ground shield on the 5_13_j1 chip in Figure 3.6. This indicates that there may be some satellite drops (secondary drops that form along with the main drop) deposited in unwanted areas, i.e.

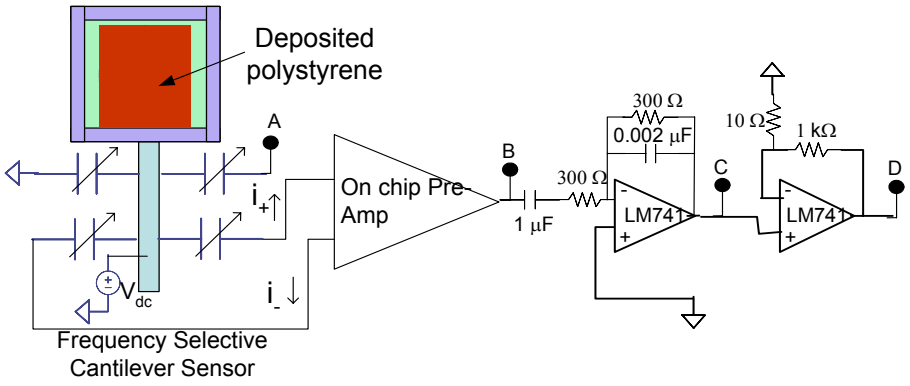

FIGURE 3.7 *Resonator with phase and gain compensation circuit*

outside of the plate. There may be some polymer bridging between the device and undercut silicon. The actual reason for the inability to operate the device after as many as 57 drops has yet to be explored. The result for the 31 drops, corresponding to a calculated 2.3 pL of polystyrene, on the 2_10_j2 resonator device experiment proved to be successful, i.e. the device could still be actuated after drops were deposited on the device.

Figure 3.7 shows the final schematic that was used in the oscillation loop. The cantilever and on-chip preamplifier are connected to two inverting operational amplifiers. Figure 3.8 shows the frequency response of the 2_10_j2 device using a network analyzer with a beam dc voltage of V_b = 20 V. The input signal into the device is at the drive right electrode, node A in

Figure 3.7, and is a 0.5 V peak to peak sinusoidal signal. The output is from the on-chip preamplifier single-ended output, node B in Figure 3.7. The left comb drive electrode was grounded. This device had a resonance frequency of 5.46 kHz and Q = 56. The magnitude and phase of the output from the pre-amplifier were -40.4 dB and 93 °, respectively.

To determine the drive signal feedthrough component the potential across the comb sensing fingers is set to 0 V. This means that the voltage on the cantilever should be equal to the DC bias voltage at the input to the preamplifier. This DC bias voltage is 1.3 V. The drive signal feedthrough magnitude with V_b = 1.3 V, which is V_{dc} in Figure 3.7, was found to be -63 dB.

FIGURE 3.8 *Network analyzer output of the 2_10_j2 (2.3 pL polystyrene) with, V_b = 20 V. Nodes A and B, in Figure 3.7, are the input and output, respectively.*

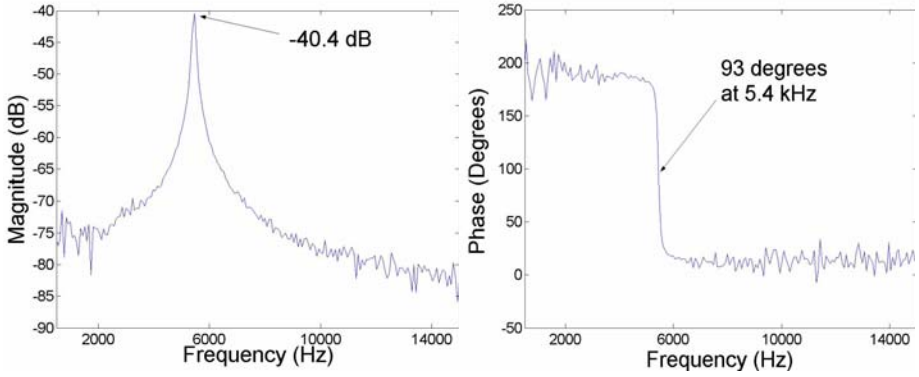

3.2.1 Adding Phase Compensation Stage

From Figure 3.8 one can see that to satisfy the criteria for oscillation a gain greater than 40 dB and a phase shift of ~ -90^{o} needs to be added to the system in order to bring the total loop gain of the system above 0 dB and the phase to 0°. The specific circuit in Section 2.7.1 was tested and it did not provide the necessary gain and phase requirements as expected for oscillation. This is probably due to unwanted parasitics from the breadboard used to construct the circuit. The phase compensation stage (with node B as the input and node C as the output) in Figure 3.7 was added to the resonator. The system has two poles at 530 Hz and 256 kHz. The second stage shown in Figure 3.7 provides the necessary gain. Figure 3.9 shows the predicted system response of the two stages (with node B as the input and node D as the output) shown in Figure 3.7.

FIGURE 3.9 *Frequency response of added components*

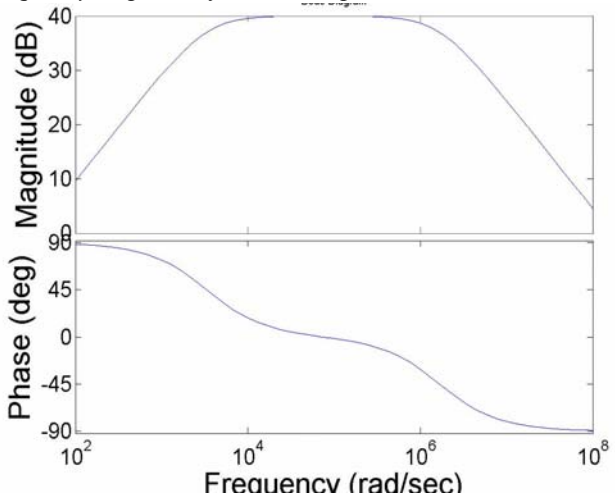

The gain and the phase of these external stages in the pass-band frequency of interest are 40 dB and 0^o, respectively.

Figure 3.10 shows the response of the system with the right comb drive electrode as the input (node A in Figure 3.7) to the system and the output (node C in Figure 3.7) is after the first compensation stage.

FIGURE 3.10 *Network analyzer transfer response (resolution bandwidth = 300 Hz) with compensation stage one output as V_{out} and comb finger drive right as V_{in} (12-12-j3 chip)*

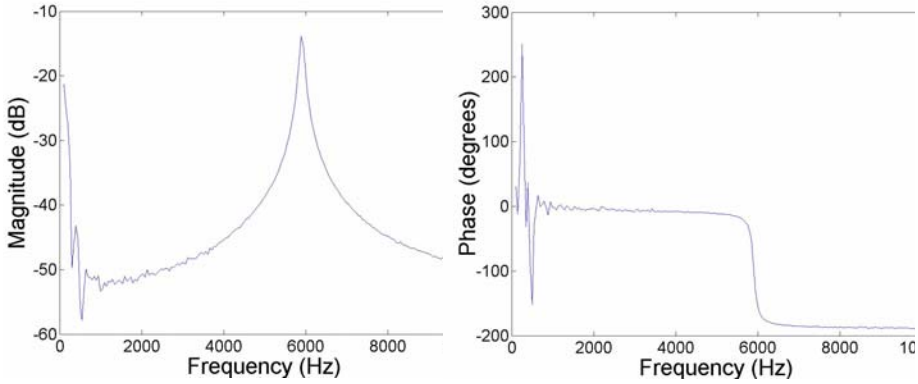

At resonance, this added stage shifted the phase of the system from 90^o to -130^o. Since it is an inverting stage the phase shift should just be -90^o since the resonance frequency is in the passband. Therefore, this stage adds an extra -40^o phase shift. Figure 3.11 shows the frequency response of the total system output at the output of the second compensation stage (node D in Figure 3.7). The second stage adds an approximate 20 dB and ~ 50^o phase shift.

FIGURE 3.11 *Network analyzer response with two compensation stages (12-12-j3 chip without polystyrene & resolution bandwidth = 300 Hz)*

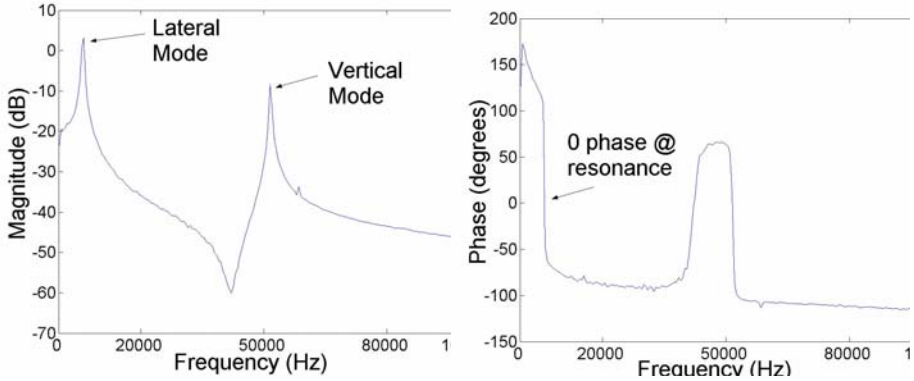

The lateral and vertical modes resonant frequencies were experimentally found to be 6.094 kHz and 51.549 kHz, respectively. Before filtering the vertical resonance mode was 3dB greater than that of the lateral mode resonance indicating that the frequency filtering of the added circuitry did reduce the magnitude of the unwanted resonant component.

The following equation was used to calculate these resonant frequencies

$$f_r = \frac{1}{2\pi}\sqrt{\frac{0.25E_{eff}\cdot h\left(\frac{w}{l}\right)^3}{m_{eff}+m_{plate}}} \tag{3.1}$$

where E_{eff} is the effective Young's modulus, h, w, and l, the height, width, and length of the beam, m_{eff}, the effective mass of the beam, and m_{plate} the mass of the end plate. The effective mass of the beam is dependent on the shape func-

tion of the beam and is 0.236*m_{beam}. The lateral mode resonance was calculated to be 10.54 kHz while the vertical resonance was calculated to be 28.68 kHz. The calculated frequencies are based on the dimensions that were drawn before fabrication at the foundry. The actual width and height of the cantilever has not been measured experimentally.

Figure 3.12 shows the configuration used for oscillation and Figure 3.13 shows the spectrum analyzer output (at node B in Figure 3.12) at oscillation. The left comb finger drive was grounded while the right was used as the feedback input from the off-chip circuitry.

FIGURE 3.12 *Oscillator schematic*

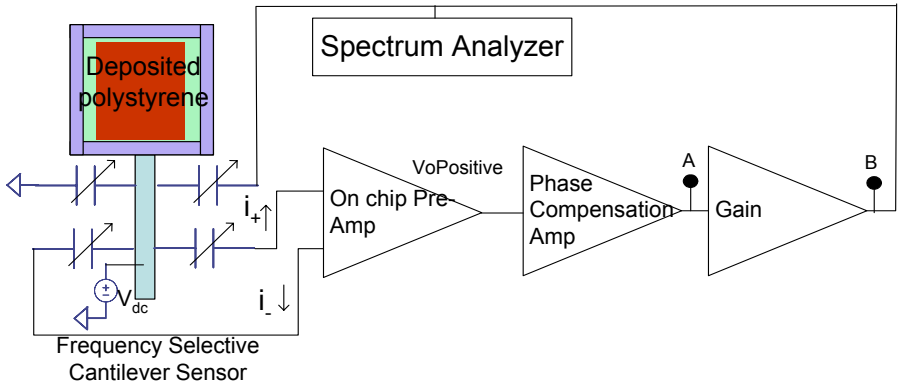

In the Jazz design, all of the bondpads have ESD diodes between the bonding pad and Vss (ground in this case). There are diodes between the driving comb

FIGURE 3.13 *12-12-j3 Oscillation output (node B in Figure 3.12) at fundamental and harmonic frequencies (12-12-j3 chip with no drops of polystyrene Vbeam = 21.8 V)*

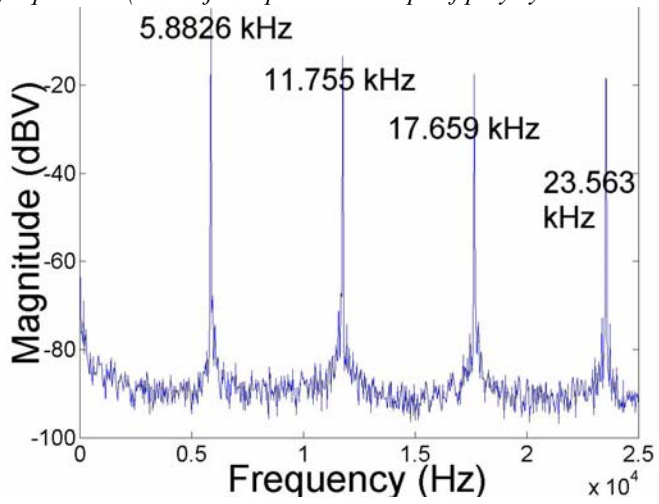

drive input (node A in Figure 3.7) and Vss as well as between the output of the on-chip pre-amp (node B in Figure 3.7). The amplitude of the oscillation signal at the driving input of the resonator is limited by this diode. The amplitude of this oscillation signal will be clipped at -0.8 V. This clipping will cause the harmonics shown in Figure 3.13. Since the frequency response at the resonant frequency in Figure 3.11 shows an open loop gain greater than 1 then the oscillation amplitude should grow without bound until it reaches the limits, i.e. the diode clipping voltage and the operational amplifier large signal output voltage swing specifications for the LM741CN operational amplifiers used. This value is typically +/- 13 V.

Since the waveform will be clipped at -0.8 V and +13 V the oscillation waveform will be a square wave with a frequency, f_r, and amplitude V_r. The Fourier expansion for such a periodic square function with an amplitude of 1 is

$$F(t) = \frac{4}{\pi} \sum_{n = 1, 3, 5, \ldots} \frac{1}{n} \sin \omega_r t \tag{3.2}$$

This expansion shows that a square wave is made up of an infinite number of sinusoidal waves. The frequencies of these sinusoidal waves are odd harmonics of the frequency of the square wave. Equation 2.71 shows that every sinusoidal frequency component, ω, generates a force term at that frequency, ω, and at twice that frequency, 2ω. Letting $A = \frac{4}{\pi} V_r$ and using the force components evaluated in (2.71) the relative magnitudes of the force components at the different harmonics are listed in Table 3.4

TABLE 3.4 *Frequency components and relative magnitudes*

Frequency	Expected Force components	Force Components (nN)	Experimentally found magnitude
ω_r	$A\frac{dC}{dx}V_b$	3.9	0.7534 V
$2\omega_r$	$\frac{A^2}{4}\frac{dC}{dx}$	0.033	0.2113 V

TABLE 3.4 *Frequency components and relative magnitudes*

$3\omega_r$	$\frac{A}{3}\frac{dC}{dx}V_b$	1.3	0.1321 V
$4\omega_r$	$\frac{\left(\frac{A^2}{4}\frac{dC}{dx}L(2\omega_r)\right)^2}{4}\frac{dC}{dx}$	0.003	0.1164 V

The magnitude of the first harmonic relative to the magnitudes of the 3rd, 5th, 7th,... should differ by a factor of 3, 5, 7,..., respectively. However, the measured 3rd harmonic relative to the 1st is 5.56. It is not clear why these values differ. It may be due to the fact that the oscillation wave is not a full square wave. It is a sinusoidal wave with an amplitude of 2.75 Volts and it is clipped at -0.8 V implying that the higher order harmonics will not have as great as a magnitude as that of full square wave.

3.3 Gas Test Measurement Setup

Figure 3.14 illustrates the gas test measurement setup used to test the gravimetric sensor. Nitrogen is the current carrier gas for gas testing. The nitrogen supply is connected to the test system through an adjustable flow-meter and a 2-way ball valve. The flow-meter has a minimum flow rate of 0.21 liters per minute (Lpm) and a maximum rate of 1.21 Lpm. One outlet of the ball valve

FIGURE 3.14 *Gas Test Setup*

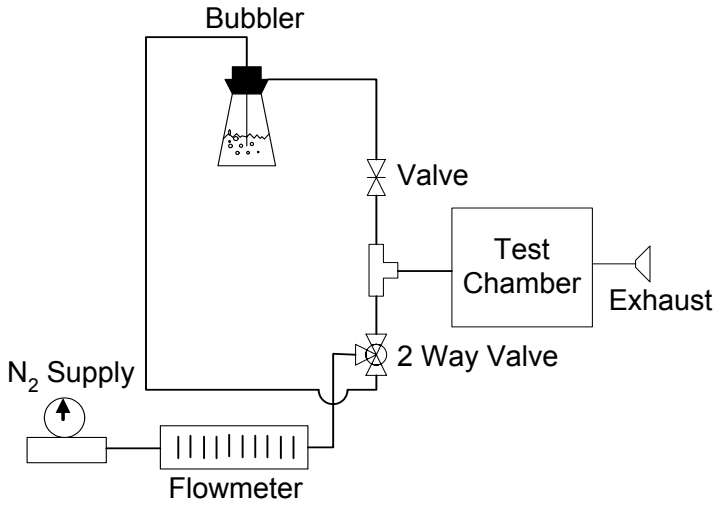

connects to a T-connector used to combine the carrier gas and analyte vapor prior to entering the test chamber. The other outlet of the ball valve is connected to the inlet of a bubbler which is submersed in the liquid form of the analyte of interest, i.e. methanol, ethanol, 2-propanol, and acetone. The outlet of the bubbler is connected to the other inlet of the T-connector. The specimen test chamber has eight coaxial cable feedthroughs for making electrical connections to the sensor. The test chamber is aluminum to provide an electrical shield around the specimens and is sealed with a gasket to prevent gas from escaping into the environment.

3.3.1 Gas test with no polymer drops using the 12-12-j3 chip

The liquid form of each specific analyte was placed in the bubbler and the frequency shift in the resonance was monitored. Measurements were taken under a nitrogen flow rate of 1 L/min and the frequency was manually recorded every 30 seconds for approximately 5 minutes in order to estimate the time response of the system. The time required for the flow of the gas through the lines and test chamber to come to equilibrium is approximately one minute. It is assumed saturation is reached in the test chamber but the exact time at which this occurs was not determined. The gases were flowed for 5-6 minutes for each gas test. Figure 3.15 through Figure 3.18 show the acetone, methanol, ethanol, and 2-propanol gas tests on the control device without polymer (12-12-j3 chip).

FIGURE 3.15 *Acetone tests on 12-12-j3 with no polymer (spectrum analyzer outputs)*

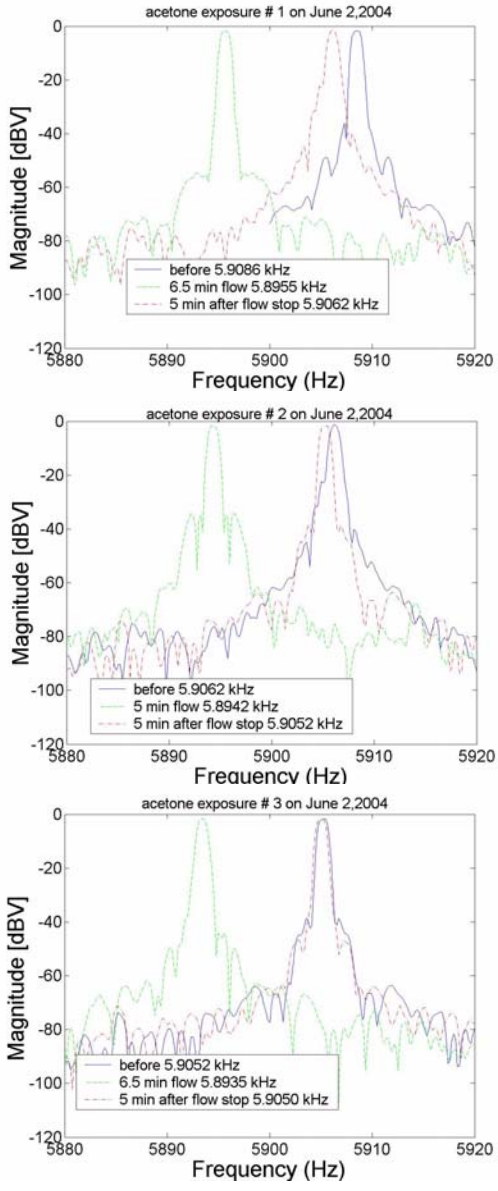

FIGURE 3.16 *Methanol tests on 12-12-j3 with no polymer (spectrum analyzer outputs)*

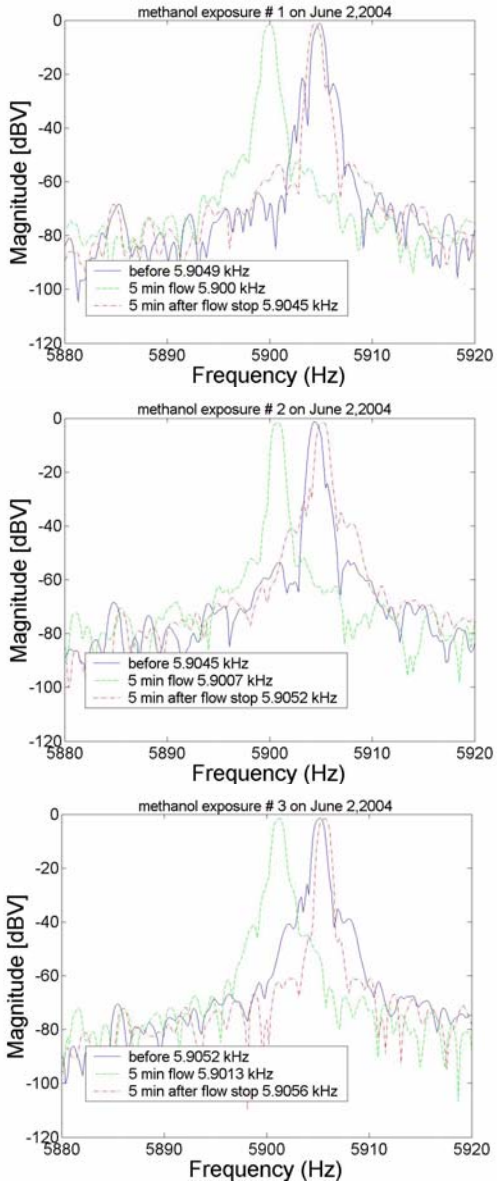

FIGURE 3.17 *Ethanol tests on 12-12-j3 with no polymer (spectrum analyzer outputs*

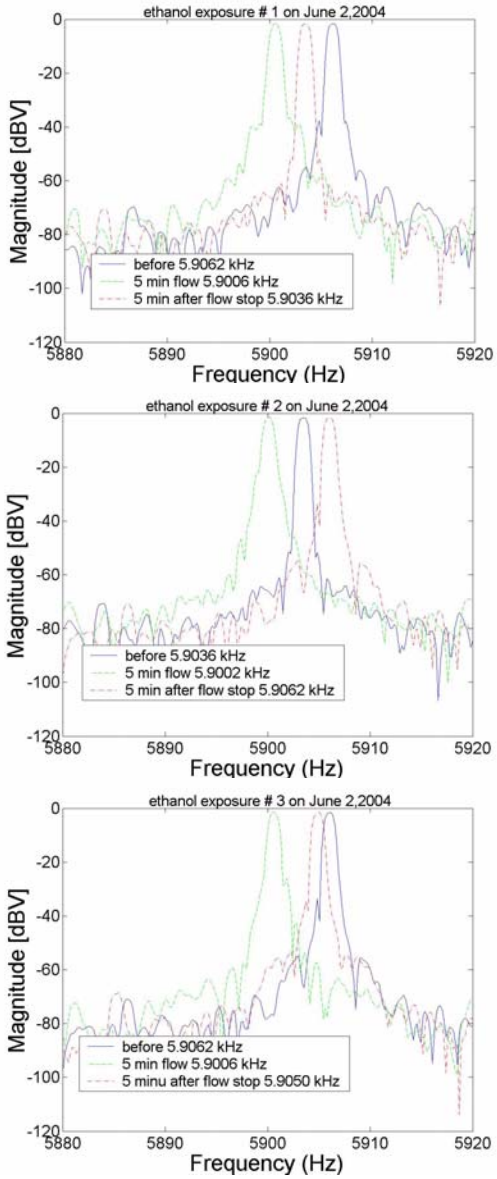

FIGURE 3.18 *2-propanol flow on 12-12-j3*

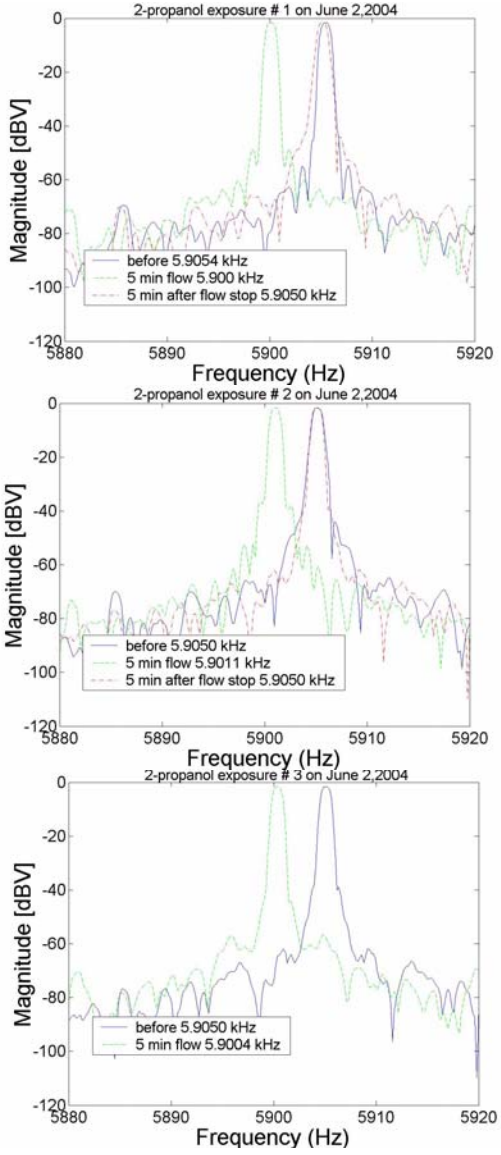

Gas flow test summary on no polymer chip (12-12-j3).

Table 3.5 through Table 3.8 summarize the frequency shifts between no exposure, 5 minutes of exposure, and then 5 minutes after turning off the analyte. All of the experiments were performed on the same day. For most of the tests the resonant frequency did not return exactly to its initial frequency value even after 5 minutes after the exposure was turned off. This may be due to the the device resonant frequency drift over time that occurs without analyte exposure. For the current device, the oscillator resonant frequency drift over time is still currently being explored. Future work in this is necessary for full device characterization.

TABLE 3.5 *Acetone before and after resonance values (Hz)*

#	start time	before exposure	@ saturation after 5 min. exposure	5 min. after exposure removed	Δ f due to exposure	Δ f between before & after exposure
1	12:09:30	5908.6	5895.5	5906.2	-13.1	-2.4
2	12:21:00	5906.2	5894.2	5905.2	-12.0	-1.0
3	12:31:00	5905.2	5893.5	5905.0	-11.7	-0.2

TABLE 3.6 *Methanol before and after resonance values (Hz)*

#	start time	before exposure	@ saturation after 5 min. exposure	5 min. after exposure removed	Δ f due to exposure	Δ f between before & after exposure
3	1:50:00	5904.9	5900.0	5904.5	-4.9	-0.4
4	2:00:00	5904.5	5900.7	5905.2	-3.8	-0.7
5	2:10:00	5905.2	5901.3	5905.6	-3.9	-0.4

TABLE 3.7 *Ethanol before and after resonance values (Hz)*

#	start time	before exposure	@ saturation after 5 min. exposure	5 min. after exposure removed	Δ f due to exposure	Δ f between before & after exposure
6	2:31:00	5906.2	5900.6	5903.6	-5.6	-2.6
7	2:41:00	5903.6	5900.2	5906.2	-3.4	+2.6
8	2:53:00	5906.2	5900.6	5905.0	-5.6	-1.2

TABLE 3.8 *2-propanol before and after resonance values (Hz)*

#	start time	before exposure	@ saturation after 5 min. exposure	5 min. after exposure removed	Δ f due to exposure	Δ f between before & after exposure
9	3:14:30	5905.4	5900.0	5905.0	-5.6	-0.4
10	3:24:30	5905.0	5901.1	5905.0	-5.4	-0.4
11	3:34:30	5905.0	5900.4	5904.6	-4.6	-0.4

3.3.2 Gas flow tests on chip with 31 drops of polystyrene (2-10-j2 chip)

Figure 3.19 through Figure 3.22 show the gas tests on the device with 2.3 pL of polystyrene. The tests on this device (2-10-j2 chip) with polystyrene was done on a different day than the tests done on the 12-12-j3 chip.

FIGURE 3.19 *Acetone tests (1-4) on 2-10-j2 chip with 31 drops polystyrene*

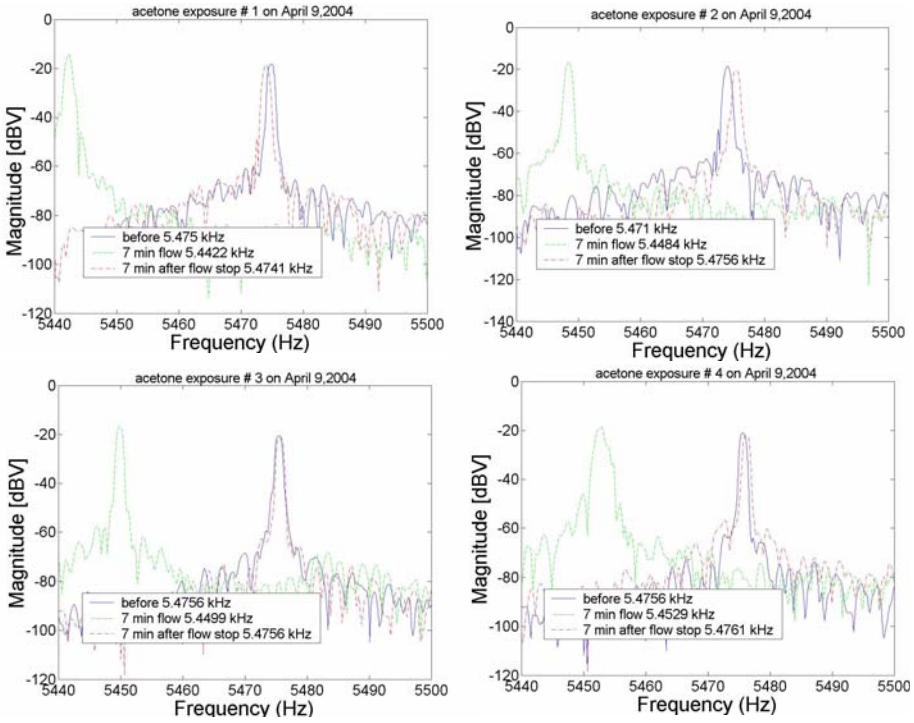

FIGURE 3.20 *Methanol tests (1-4) on 2-10-j2 chip with 31 drops of polystyrene*

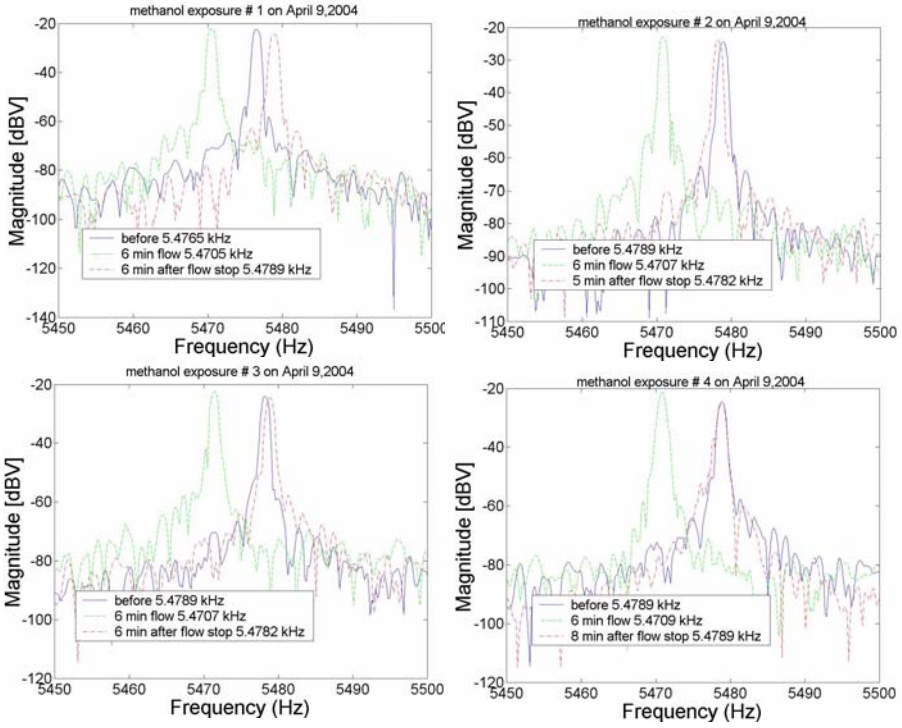

FIGURE 3.21 *Ethanol tests (1-4) on 2-10-j2 chip with 31 drops of polystyrene*

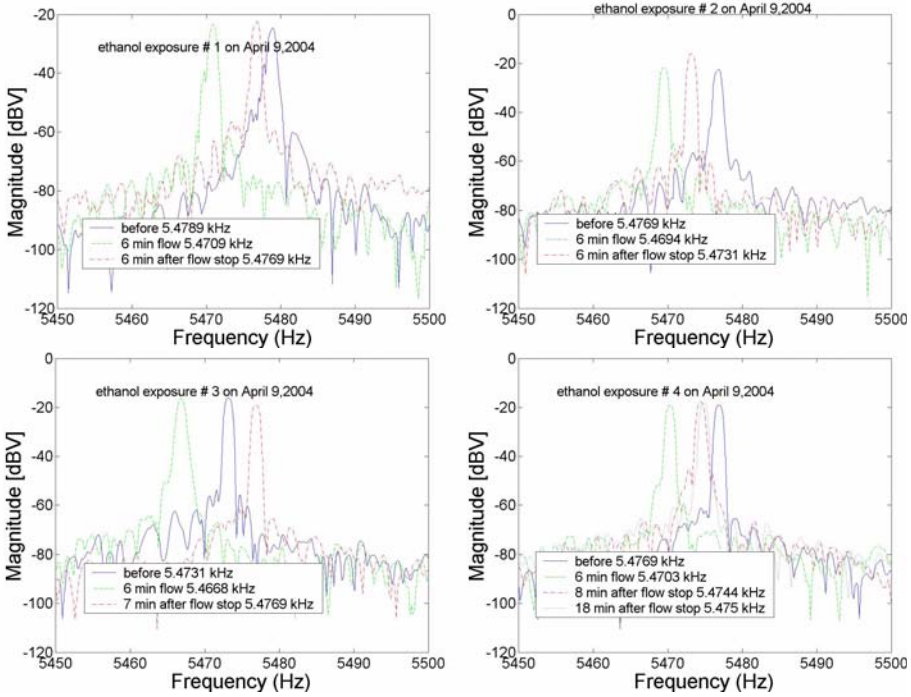

FIGURE 3.22 *2-propanol tests (2-4) on 2-10-j2 chip with 31 drops of polystyrene*

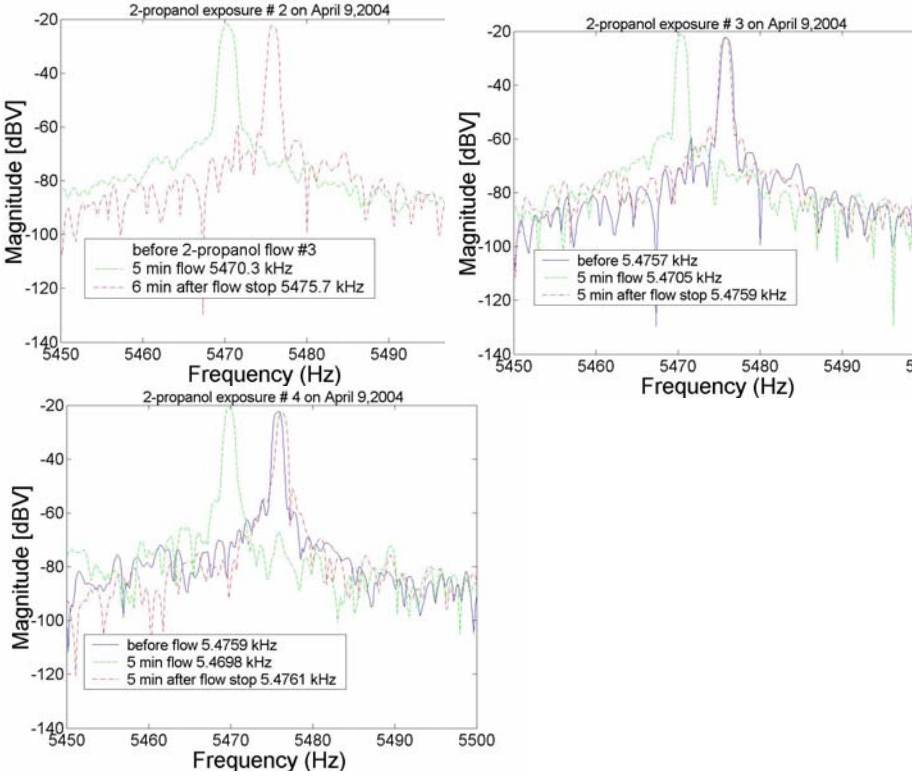

Gas flow test summary on 2-10-j2 chip with 31 drops of polystyrene.

Table 3.9 through Table 3.12 summarize the frequency shifts of the device with 2.3 pL of polystyrene between no exposure, 5 minutes of exposure, and then 5 minutes after turning off the analyte. All of the experiments shown in Figure 3.19 through Figure 3.22 were performed on the same day. Again, the resonant frequency did not return to its initial value.

TABLE 3.9 *2-propanol before and after resonance values (Hz)*

#	start time	before exposure	@ saturation after 5 min. exposure	5 min. after exposure removed	Δ f due to exposure	Δ f between before & after exposure
1	11:26:15	5477.2	5470.3	5475.7	-6.9	-1.5
2	11:39:00	5475.7	5470.5	5475.9	-5.2	+0.2
3	11:51:00	5475.9	5469.8	5476.1	-6.1	+0.2

TABLE 3.10 *Methanol before and after resonance values (Hz)*

#	start time	before exposure	@ saturation after 5 min. exposure	5 min. after exposure removed	Δ f due to exposure	Δ f between before & after exposure
4	12:08:45	5476.5	5470.5	5478.9	-6.0	+2.4
5	12:24:00	5478.9	5470.7	5478.2	-8.2	-0.7
6	12:36:00	5478.9	5470.7	5478.2	-8.2	-0.7
7	12:49:00	5478.9	5470.9	5478.9	-8.0	0.0

TABLE 3.11 *Ethanol before and after resonance values (Hz)*

#	start time	before exposure	@ saturation after 5 min. exposure	5 min. after exposure removed	Δ f due to exposure	Δ f between before & after exposure
8	1:05:15	5478.9	5470.9	5476.9	-8.0	-2.0
9	1:18:00	5476.9	5469.4	5473.1	-7.5	-3.8
10	1:31:30	5473.1	5466.8	5476.9	-6.3	+3.8
11	1:45:00	5476.9	5470.3	5475.0	-6.6	-1.9

TABLE 3.12 *Acetone before and after resonance values (Hz)*

#	start time	before exposure	@ saturation after 5 min. exposure	5 min. after exposure removed	Δ f due to exposure	Δ f between before & after exposure
12	2:10:00	5475.0	5442.2	5474.1	-32.8	-0.9
13	2:24:15	5471.0	5448.4	5475.6	-22.6	+4.6
14	2:38:15	5475.6	5449.9	5475.6	-25.7	0.0
15	2:52:15	5475.6	5452.9	5476.1	-22.7	+0.5

3.4 Device Sensitivity to the Different Gases

The frequency shift due to each gas was averaged over the experiments and the resulting sensitivity (Hz/ppm) for each particular analyte was derived assuming that the 5 minute exposure frequency shifts were at a saturated concentration in the test chamber. Concentration (in ppm) of analyte, A, at saturation are derived in the following manner assuming STP (25 ^{o}C @ 1 atm = 760 mmHg)

$$Concentration_A = \frac{P_A}{760\text{mmHg}} \cdot 10^6 \tag{3.3}$$

Table 3.13 shows the saturation levels of the particular analytes used for this work given the vapor pressure values listed in Table 2.1

TABLE 3.13 *Concentration (ppm) of various analytes at saturation*

Analyte	Saturation Level (ppm)
acetone	303,990
methanol	166,800
ethanol	77,671
2-propanol	59,408

Table 3.14 shows the resulting sensitivities (Hz/ppm) for the two gravimetric devices, 12-12-j3 and 2-10-j2 devices.

TABLE 3.14 *Average experimentally determined sensitivity values for device with and without polystyrene*

Analyte	Average Sensitivity w/o polystyrene (Hz/ppm)	Average Sensitivity w/ 31 drops of polystyrene (Hz/ppm)
acetone	-0.0000403	-0.0000854
methanol	-0.0000258	-0.0000456
ethanol	-0.0000627	-0.0000914
2-propanol	-0.0000875	-0.0001021

From (2.50), the expected sensitivity for a particular analyte is calculated using (3.4) and presented in Table 3.15.

$$J = -\frac{1}{4\pi}\frac{\sqrt{k}}{\sqrt{\left(m_o + \frac{4}{3}\pi R_{drop}^3 C_{drop} N_{drop}\right)^3}}\left(\frac{4}{3}\pi R_{drop}^3 C_{drop} N_{drop}\right)\left(\frac{1}{K_{AP}}\right)\left(\frac{1}{\rho_{poly}}\right) \qquad (3.4)$$

The calculations use parameter values of 31 drops of polystyrene at a radius of 20 μm, C_{drop} of 2 mg/mL, k = 0.298 N/m, m_o = 2.517 x 10^{-10} kg, and K_{AP} and density values from Table 2.2.

TABLE 3.15 *Expected sensitivity values, (from Table 2.3) with 31 drops of polystyrene, versus experimentally observed values of device 2-10-j2.*

Analyte	Expected Sensitivity (Hz/ppm)	Experimental Sensitivity (Hz/ppm)
acetone	-0.0064	-0.0000854
methanol	-0.0081	-0.0000456
ethanol	-0.0120	-0.0000914
2-propanol	-0.0133	-0.0001021

The expected and experimental sensitivities are calculated with the assumption that the gas saturation concentration level in the chamber for the corresponding analyte has been reached at 5 minutes of exposure. This may, in fact, not be the case. Further tests using known gas concentration levels may give sensitivity values closer to theory. Figure 3.23 shows that there does not appear to be correlation between experimental sensitivity and the theoretical solubility of the analyte in polystyrene. However, the expected sensitivity should increase with solubility, which is dependant upon the vapor pressure of the gas. In the gas tests, the chamber may not have been completely purged between gas tests. The purge time between tests was 5 minutes. This would

result in gas mixtures in the chamber and then the affinity of polystyrene to certain analytes over the others becomes a variable in the analysis. Better controlled gas concentration experiments are, therefore, necessary for proper analysis.

FIGURE 3.23 *Experimental sensitivity versus expected solubility of the analyte in polystyrene for 31 drops*

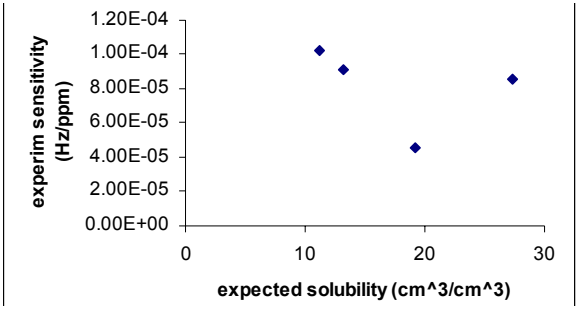

3.5 Resonator with capillary channel

There has been some current work delving into a device configuration that exploits the ink jet drop characteristics. A first generation design has been submitted and verified as a viable means of placing small amounts of polymer on a small resonator using the ink jet process. Figure 3.24 shows a SEM of such a device. The device actuation and sensing configuration is just like the current device described in this report. However, there is a well placed at the anchor of the resonator and the end plate is removed. This well serves as the

FIGURE 3.24 *Beam with channel (a) with enlarged view at the anchor point (b) for placement of polymer using the ink jet drops*

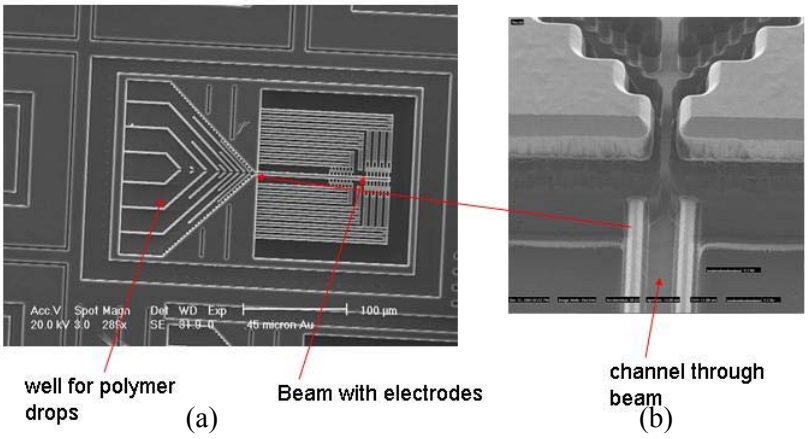

target for ink jet drops and contains capillary channels to direct the solution towards a channel along the beam, which is illustrated in Figure 3.24. Six drops of polystyrene were deposited in this well and the following images show the dried polystyrene along the channel of the resonator, which resulted due to solution drawn into the channel beam via capillary action. This design proved successful in placing polymer on the beam without affecting the electrostatic gaps nearby. Device characterization and analysis as a gas sensor is underway.

FIGURE 3.25 *Beam with capillary channel before (a) and after (b) 6 drops of polystyrene (2 mg/mL in 1 toluene:1 xylene solution)*

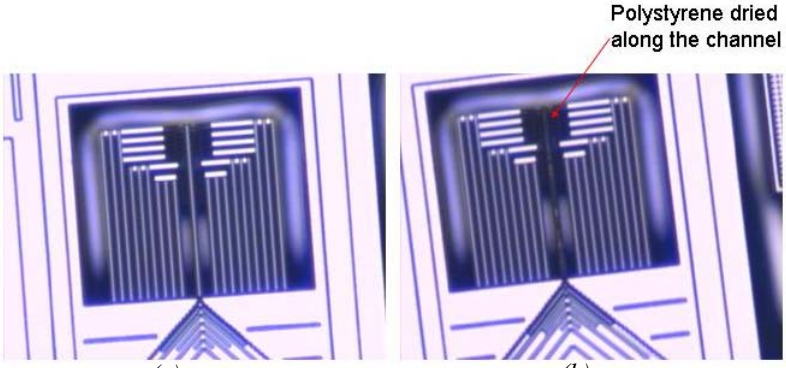

(a) *(b)*

4 Discussion & Conclusions

4.1 Discussion

A self-excited resonator oscillator implemented in a CMOS/MEMS technology acting as an organic vapor detector has been successfully demonstrated. The device was tested without and with a calculated 2.3 pL of polystyrene on the cantilever end plate. Methanol, ethanol, 2-propanol, and acetone in a nitrogen carrier gas were the analytes tested.

The device tested without polymer responded to the analytes. The resonant frequency shift probably occurs when the analyte absorbs onto the surface of the device. Post-processing conditions induce some organic polymers to accumulate onto the devices. It is not known how much of this polymer accumulates during the process nor is its concentration known but this substance may also act as chemical receptor layer. It was also observed that the

resonance frequency does not exactly return to its initial value after analyte exposure for either of the devices, with or without the polystyrene. Both net positive and negative frequency shifts, after the removing analyte, were observed. There was no apparent correlation between this shift and the analyte type because both types of shifts were observed for all analytes. This phenomena may be due to several factors. First of all, the environment of the device under test was not well controlled in this initial work. The exact concentration levels of the gas flowed is not known. Therefore, there may have been some residual gas in the system from the previous analyte test. Subsequently, these shifts may depend on what was previously flowed through the system. The device will respond differently to mixtures of gases accordingly due to different affinities for different analytes. These problems should be alleviated with a well controlled gas test system, which is under construction. Also, the humidity of the environment may affect the absorption and desorption rates of analytes. Device response to humidity levels has yet to be explored.

The measured analyte absorbed was greater for the device with 2.3 pL of deposited polystyrene than the device without polystyrene. The sensitivity to acetone and methanol was doubled with polystyrene while the sensitivities to ethanol and 2-propanol increased by 50%. The highest frequency shift

occurred with exposure to acetone because of it is inherently higher vapor pressure and, therefore, higher ambient concentration at saturation levels. Also, the solubility of the gas in the "glassy" polystyrene polymer increases with vapor pressure. The sensitivities to the different analytes is expected to increase with increasing vapor pressure. However, the experimental results did not show a consistent trend with vapor pressure variations. A wider range of gases and gas concentrations are needed to better quantify this trend.

For the sake of comparison, we note that the contemporary work, involving dynamic mode gravimetric sensors, by Lange et al. [4] showed sensitivity levels of -0.01 Hz/ppm to ethanol using polyetherurethane as the sensitive layer. The experimental results for this work using polystyrene as the sensitive layer show an average sensitivity of -9.14×10^{-5} Hz/ppm to ethanol. The theoretically calculated limit of sensitivity to ethanol of the current device configuration with 54 pL of polystyrene, which is equivalent to 806 drops of polystyrene from a 2mg/mL solution of 1:1 toluene:xylene, is calculated to be -0.13 Hz/ppm. This derived value was calculated with the assumption that the maximum amount of polystyrene on the end plate of the device is limited to 54 pL of this polymer. It is not apparent whether this maximum limit of volume of polystyrene can be placed on the device because even 4.2 pL of poly-

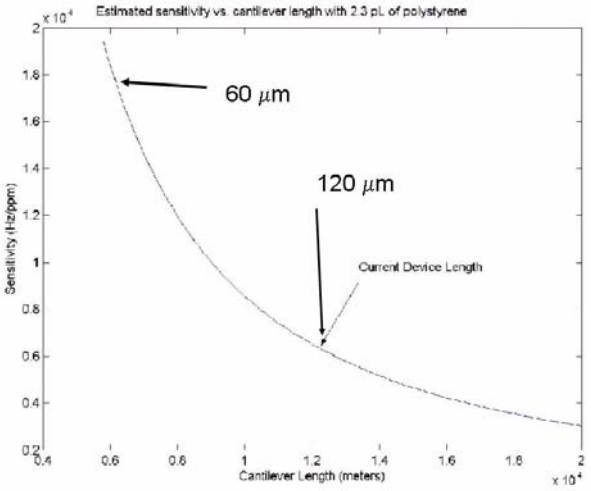

FIGURE 4.1 *Cantilever sensitivity vs. cantilever length with 2.3 pL of polystyrene*

styrene inhibited the current device from being actuated. Future investigations of this issue must be undertaken.

However, using the current configuration, i.e. the same end plate size, the same pitch and number of comb fingers in the drive and sensing capacitors, the reduction of the length to 60 μm of the resonator would result in a higher resonance frequency and ultimately higher device mass sensitivity (Hz/gram). Figure 4.1 shows a plot of how the sensitivity would improve with a decrease in the cantilever length. This proposed length change and the use of the same volume, 2.3 pL, of polystyrene on this future device will lead to a calculated -

0.03 Hz/ppm sensitivity to ethanol. Using the maximum volume, 54 pL, of polystyrene on the end plate of this future device should result in a -0.37 Hz/ppm concentration sensitivity to ethanol.

4.2 Future Work

Future work should involve several factors such as full optimization of the device configuration as discussed above, determination of the frequency stability (i.e. short and long term variation in oscillation frequency which is dependant on the cantilever and feedback system) of the oscillator and, subsequently, estimating the limits of detection, quantification of the exact amounts of polymer deposited using the ink jet, exploration of other device configurations that may exploit the post-processing ink jet drop characteristics which is described in Section 3.5, and exploration of other types of chemically sensitive polymers to obtain higher sensitivities and selectivities to other gases. Overall, the current work has demonstrated a successful implementation of a gravimetric gas sensor using the CMOS/MEMS technology and has provided us with direction for future device design and testing methods.

Bibliography

[1] J. R. Stetter and W. R. Penrose, “Understanding Chemical Sensors and Chemical Sensor Arrays (Electronic Noses): Past, Present, and Future”, Sensors Update, Baltes, H., Fedder, G. K., Korvink, J. G., Eds., vol. 4, p. 189-229, 2002.

[2] A. Hierlemann and H. Baltes, “CMOS-based chemical microsensors”, Analyst, 128, p. 15-28, 2003.

[3] Patel, R., Zhou, R. Zinszer, K., and F. Josse, “Real-time detection of organic compounds in liquid environments using polymer-coated thickness shear mode quartz resonators”, *Analytical Chemistry*, vol. 72, no. 20, p. 4888-4898, 2000.

[4] Lange, D., Hagleitner, C., Hierlemann, A., Brand, O., and H. Baltes, “Complementary Metal Oxide Semiconductor Cantilever Arrays on a Single Chip: Mass-Senstive Detection of Volatile Organic Compounds”, *Analytical Chemistry*, vol. 74., no. 13, p. 3084-3095, 2002.

[5] Bodenhofer, K., Hierlemann, A., Noetzel, G., and W. Gopel, “Performances of mass-sensitive devices for gas sensing: thickness shear mode and surface acoustic wave transducers”, *Analytical Chemistry*, vol. 68, no. 13, p. 2210-2218, 1996.

[6] Baller, M. K., Lang, H. P., Fritz, J., Gerber, Ch., Gimzewski, J. K., Drechsler, U., Rothuizen, H., Despont, M., Vettiger, P., Battiston, F. M., Ramseyer, J. P., Fornaro, P., Meyer, E., and H. J. Guntherodt, “A cantilever array-based artificial nose”, *Ultramicroscopy*, 82, p. 1-9, 2000.

[7] Battiston, F. M., Ramseyer, J. P., Lang, H. P., Baller, M. K., Gerber, Ch., Gimzewski, J. K., Meyer, E., and H. J. Guntherodt, “A chemical sensor based on a microfabricated cantilever array with simultaneous resonance-frequency and bending readout”, *Sensors and Actuators B,* 77, p. 122-131, 2001.

[8] Jensenius, H., Thaysen, J., Rasmussen, A., Veje, L. H., Hansen, O., and A. Boisen, “A microcantilever-based alcohol vapor sensor-application and response model”, *Applied Physics Letters*, vol. 76, no. 18, p. 2615-2617, 2000.

[9] Fritz, J., Baller, M. K., Lang, H. P., Rothuizen, H., Vettiger, P., Meyer, E., Guntherodt, H. J., Gerber, Ch., and J. K. Gimzewski, “Translating biomelecular recognition into nanomechanics”, *Science*, 288, p. 316-318, 2000.

[10] Berger, R., Delamarche, E., Lang, H. P., Gerber C., Gimzewski, J. K., Meyer, E., Guntherodt, H., "Surface Stress in the Self-Assembly of Alkanethiols on Gold", *Science*, 276, p. 2021-2024, 1997.

[11] Schierbaum, K. D., Gerlach, A., Haug, M., and W. Gopel, "Selective detection of organic molecules with polymers and supramolecular compounds: application of capacitance, quartz microbalance, and calorimetric transducers", *Sensors and Actuators A*, 31, p. 130-137, 1992.

[12] Ricco, A. J., Kepley, L. J., Thomas, R. C., Sun, L., and R. M. Crooks, "Self-assembling monolayers on SAW devices for selective chemical detection", *IEEE Solid-State Sensor & Actuator Workshop-Hilton Head, S.C. June 22-25*, p. 114-117, 1992.

[13] O. Brand and H. Baltes, "Micromachined Resonant Sensors-an Overview", *Sensors Update*, Baltes, H., Gopel, W., and Hesse, J. Eds., VCH: Weinheim, Germany, vol. 4, p.36, 1998.

[14] G. K. Fedder, S. Santhanum, M.L. Reed, S. C. Eagle, D. F. Guillou, M. S. C. Lu, and L. R. Carley, "Laminated high-aspect-ratio microstructures in a conventional CMOS process," *Proceedings of the 9th IEEE International Workshop on Micro Electro Mechanical Systems (MEMS '96),* San Diego, CA, February 15-17, 1996, pp. 13-18.

[15] Jazz Semiconductor website, http://www.jazzsemi.com/process_technologies/sige.shtml, 4321 Jamboree Rd., Newport Beach, CA 92660.

[16] MOSIS website, http://www.mosis.com/products/fab/vendors/tsmc/, MOSIS Integrated Circuit Fabrication Service, USC Information Sciences Institute, 4676 Admiralty Way, 7th floor, Marina del Rey, CA 90292-6695.

[17] S. Senturia, "Microsystem Design", Boston: Kluwer Academic Press, 2001.

[18] Davis, Z. J., Abadal, G., Helbo, B., Hansen, O., Campabadal, F., Perez-Murano, F., Esteve, J., Figueras, E., Ruiz, R., Barniol, N., Boisen, A., "High mass and spatial resolution mass sensor based on resonating nano-cantilevers integrated with CMOS", *Proceedings of Transducers '01*, Munich 2001, pp. 72-25.

[19] Albrecht, T. R., Grutter, P., Horne, D., and e. Rugar, "Frequency modulation detection using high-Q cantilevers for enhanced force microscope sensitivity", *Journal of Applied Physics*, vol. 69, No. 2, p. 668, 1991.

[20] Zhang, W., Baskaran, R., and K. L. Turner, “Effect of cubic nonlinearity on auto-parametrically amplified resonant MEMS mass sensor”, Sensors and Actuators A 102 (2002) 139-150.

[21] B. Razavi, "Design of Analog CMOS Integrated Circuits", Boston: McGraw Hill, 2001.

[22] W. C. Tang, T. C. H. Nguyen and R. T. Howe, Laterally driven polysilicon resonant microstructures, IEEE Micro Electro Mechanical Systems Workshop, Salt Lake City, UT, U.S.A., Feb. 20-22, 1989. pp. 53-59.

[23] H. Luo, “Integrated multiple device CMOS-MEMS IMU systems and RF MEMS applications”, *Ph D. Thesis,* Dept. of Electrical and Computer Engineering, Carnegie Mellon University, Dec. 17, 2002.

[24] J. Brotz, “Damping in CMOS-MEMS Resonators”, *M.S. Thesis,* Dept. of Electrical and Computer Engineering, Carnegie Mellon University, June 2004.

[25] P. Y. Bruice, “Organic Chemistry: Second Edition”, New Jersey: Prentice Hall, 1998.

[26] M. Chanda and Roy, S. K., “Plastics Technology Handbook: Second Edition, Revised and Expanded”, New York: Marcel Dekker, 1993.

[27] MicroFab Technologies, Inc., http://www.microfab.com/equipment/index.html, 1104 Summit Ave., Suite 110, Plano, TX 75074.

[28] R. N. Haward, “The Physics of Glassy Polymers”, New York: John Wiley & Sons, 1973.

[29] Van Krevelen D.W., “Properties of Polymers: Their Estimation and Correlation with Chemical Structure”, Amsterdam: Elsevier Scientific, 1976.

[30] Lide, D. R. (Editor-in-Chief), “CRC Handbook of Chemistry and Physics: 77th Edition”, Boca Raton: CRC Press, 1996.

[31] Kotz, J. C. and Treichel, P., “Chemistry and Chemical Reactivity: Fourth Edition”, Fort Worth: Sauders College, 1999.

[32] Boethline, R. S. and Mackay, D., “Handbook of Property Estimation Methods for Chemicals: Environmental and Health Sciences”, Boca Raton, Florida: Lewis Publishers, 2000.